minerals

MDPI

Article

Petrogenesis of Alkaline Complex of the Longbaoshan Rare Earth Element Deposit in the Luxi Block, North China Craton, China

Ze-Yu Yang [1], Shan-Shan Li [1], Mao-Guo An [1,2], Cheng-Long Zhi [1,2], Zhen Shang [2], Zheng-Yu Long [1], Jian-Zhen Geng [1,3], Hao-Cheng Yu [1] and Kun-Feng Qiu [1,2,*]

[1] State Key Laboratory of Geological Processes and Mineral Resources, School of Earth Sciences and Resources, China University of Geosciences, Beijing 100083, China
[2] Shandong Provincial Lunan Geology and Exploration Institute (Shandong Provincial Bureau of Geology and Mineral Resources No.2 Geological Brigade), Jining 272100, China
[3] Tianjin Center of China Geological Survey, Tianjin 300170, China
* Correspondence: kunfengqiu@cugb.edu.cn

Abstract: The alkaline complex in the southwest region of Luxi Terrane of the North China Craton is spatially correlated with the newly discovered Longbaoshan REE deposit. Its petrogenesis, however, remains ambiguous. In this study, we present an integrated petrology, whole-rock geochemistry, sphene U-Pb and rare earth element data from the Longbaoshan alkaline complex to investigate the petrogenesis, magma source and tectonic evolution. The Longbaoshan alkaline complex consists of mafic to intermediate rocks of hornblende diorite and alkaline hornblende syenite porphyry, biotite monzonite porphyry and aegirine diorite porphyrite. The hornblende diorites show a composition of low SiO_2, high MgO, Fe_2O_3 and moderate Na_2O, CaO and are metaluminous and medium-to-high-K calc-alkaline. The hornblende syenite porphyries, biotite monzonites and argirine diorite porphyrites display a relatively higher content of SiO_2, Na_2O, K_2O and Al_2O_3 and lower contents of MgO, Fe_2O_3 and CaO and are metaluminous, peralkaline, high-K calcic-alkaline and shoshonite. The sphene U-Pb data shows that the parent magma of the hornblende diorite was emplaced at ca. 120 Ma. All these samples show a common depletion in Th, Nb-Ta and Zr-Hf and enrichment in large ion lithophile elements (e.g., Pb, Ba, Sr) and Light Rare Earth Elements. The magma may have experienced fractionation of pyroxene, amphibole, sphene, apatite and zircon during its evolution. The variable La content, La/Sm, Rb/Sr and $(Ta/Th)_N$ ratios indicate that the parent magma may produce by partial melting of a mantle source that was interacted with sediment-derived melts in a subduction setting. Therefore, we propose that the parent magma of the Longbaoshan alkaline complex was derived from a lithospheric mantle which was metasomatized by sediment-derived melt in a prior subduction process. The enriched magma was emplaced through an extension process and experienced subsequent fractionation and assimilation with the continental crust during the rollback of the Paleo Pacific Ocean plate.

Keywords: sphene U-Pb geochronology; whole-rock and sphene geochemistry; early Cretaceous REE mineralization; newly discovered Longbaoshan deposit; North China Craton

Citation: Yang, Z.-Y.; Li, S.-S.; An, M.-G.; Zhi, C.-L.; Shang, Z.; Long, Z.-Y.; Geng, J.-Z.; Yu, H.-C.; Qiu, K.-F. Petrogenesis of Alkaline Complex of the Longbaoshan Rare Earth Element Deposit in the Luxi Block, North China Craton, China. *Minerals* **2022**, *12*, 1524. https://doi.org/10.3390/min12121524

Academic Editor: Massimo D'Antonio

Received: 30 October 2022
Accepted: 22 November 2022
Published: 28 November 2022

1. Introduction

The alkaline rocks occur in a variety of tectonic settings, such as continental rift valleys, divergent continental margins, oceanic and continental intraplates and subduction zones [1–4]. Generally, the parent magma of the alkaline rocks is derived from an enriched mantle. Therefore, the geochemistry characteristics of these alkaline rocks may preserve the mantle information [5,6]. However, the petrogenesis of the alkaline rocks remains controversial. Previous investigators have suggested that the alkaline magmas may be generated through partial melting of a metasomatized lithospheric mantle without assimilation and fractional crystallization (AFC), or magma mixing or fluid-rock interaction [7–9].

However, Chen et al. [10] suggested that the alkaline magmas may derive from a depleted mantle and experienced fractional crystallization. Moreover, some workers indicated that the parent magma of the alkaline rocks may be produced from a mantle-derived mafic magma source by fractional crystallization with or without crustal assimilation or magma mixing [1,10–16].

The North China Craton (NCC) is one of the oldest continental cores in the world and is the largest craton in China [17,18]. The craton experienced destruction during the Mesozoic, resulting in the old lithospheric mantle being replaced by a juvenile and fertile lithospheric mantle associated with the lithosphere thinning and large-scale magmatism during the Early Cretaceous [19–25]. The Luxi Terrane is located in the southeast of the North China Craton, which underwent subduction of the Paleo-Pacific plate during the Jurassic, and subsequent extension in the Early Cretaceous associated with a series of alkaline granite magmatism and rare earth element mineralization [26–30]. These rare earth element (REE) deposits are composed of the Weishan, Longbaoshan and Guandimiao deposits [31–36].

Previous petrogenetic studies suggested that the Longbaoshan alkaline complex was formed by fractional crystallization and assimilation [33]. In terms of the magma source, the similar Sr, Nd and Pb isotopic compositions of the alkaline rocks from the Longbaoshan alkaline complex and the nearby high Mg adakitic mafic rocks indicate a mantle source region [33,35]. The mantle source was considered metasomatized by a subducted material-derived fluids [33], but the nature of this fluid remains unclear. In addition, previous studies proposed that the parent magma of the alkaline complexes in the nearby Guandimiao complex was formed by partial melting of an enriched mantle source [36]. It remains enigmatic whether the parent magma of the Longbaoshan alkaline complex is influenced by partial melting. In this contribution, we present new petrology, whole-rock major and trace elements, sphene trace elements and U-Pb data from the Longbaoshan alkaline complex to place constraints on the petrogenesis, magma source and tectonic evolution.

2. Geological Setting

The Luxi Terrane is located in the southeast margin of the North China Craton (Figure 1a), which intersects to the west with the Liaocheng-Lankao Fault Zone, to the east with the Tan-Lu Fault Zone, to the south with the Fengpei fault and to the north with the Qihe-Guangrao fault [37]. The terrane experienced multiple tectonic events that formed the Archean basement including gneisses, amphibolite and Trondhjemite-Tonalite-Granodiorite (TTG), Paleoproterozoic granitoids, and are overlayed by Palaeozoic carbonates and clastic rocks, Mesozoic and Cenozoic clastic rocks, volcaniclastics, intermediate-basic igneous rocks, mafic dykes, carbonatites, and alkaline rocks (Figure 1b) [38]. The North China Craton was thinned through the Yanshan movement, resulting in a large-scale magmatism and mineralization during the Mesozoic [39–43]. The Mesozoic magmatic rocks and mineralization in the Luxi Terrane formed during this tectonic activity. The mineral resources in the region are mainly REE, gold and iron [44–49].

The Longbaoshan alkaline complex exposes in an area of ca. 2.5 km^2 in the southeastern part of the Luxi Terrane, west of the south section of Yishu Fault Zone and southeast of Nishan uplift (Figure 1b). From bottom to top, the strata include the Archaean granitic gneisses, Cambrian limestone, Ordovician limestone and dolomite and Quaternary sediments [52]. The late Paleozoic strata are widely distributed throughout the Longbaoshan area. According to the direction distribution, the faults in this region are mainly divided into four groups with an orientation of NW, NNE, EW and NS (Figure 1c).

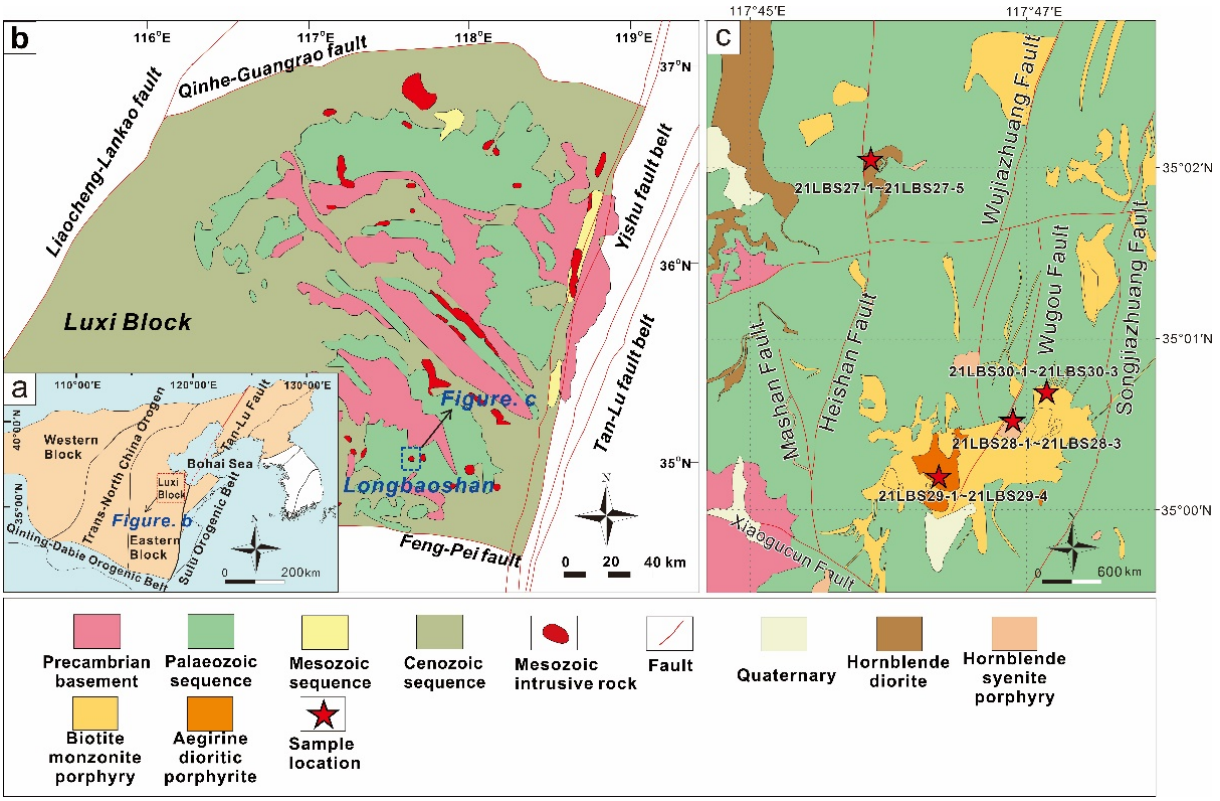

Figure 1. (**a**) Simplified geological map of eastern China and the location of Luxi Terrane, modified after [19]. (**b**) Sketch geological map of the eastern Luxi Terrane, modified after [50,51]. (**c**) Geological sketch of the Longbaoshan alkaline complex.

3. Analytical Methods

3.1. Sphene LA-ICP-MS U-Pb Dating and REE Composition Analysis

Sphene LA-ICP-MS U-Pb analyses were conducted at the Isotopic Laboratory, Tianjin Center, China Geological Survey. Laser analysis was performed using a Neptune double focusing multiple-collector ICP-MS (Thermo Fisher Ltd.) attached to a NEW WAVE 193 nm-FX ArF Excimer laser-ablation system (ESI Ltd.). The range of mass number is 4–310 amu; resolution greater than 450 (flat peak, 10% peak valley definition); the abundance is less than 5 ppm (without RPQ) and less than 0.5 ppm (with RPQ) [53].

The ion optical path of the multi receiver inductively coupled plasma mass spectrometer used in this dating work adopts the double focusing design of energy focusing and mass focusing and uses dynamic zoom to expand the mass dispersion to 17%. The instrument is equipped with 9 Faraday cup receivers and 4 ion counter receivers. In addition to the central cup and ion counter, the other 8 Faraday cups are configured on both sides of the central cup and accurately adjusted by motor drive. Four ion counters are bound to L4 Faraday cup. The laser ablation system used is the new wave193 nm fxarf excimer laser produced by ESI company of the United States. The wavelength is 193 nm, the pulse width is less than 4 ns and the beam spot diameters are 2, 5, 10, 20, 35, 50, 75, 100 and 150 μm adjustable, pulse frequency 1–200 Hz continuously adjustable, laser output power 15 J/cm^2. Detailed analytical procedures are given in [54].

In this paper, the sampling method of sample test is point ablation, and the beam spot of laser denudation is 35 μm. The frequency is 8 Hz and the energy density is 11 J/cm^2. The laser denuded material is sent to ICP-MS with He as the carrier gas. NIST SRM 610 glass and NIST SRM 612 glass were used as external standards to calculate U, Th, and Pb concentrations of sphenes. MKED1 and OLT1 were used as internal standards for monitoring the stability and accuracy of the instrument and acquired U-Pb data. The results of standard measurements are 1519.7 ± 4.4 Ma (n = 12, MSWD = 0.29) for the MKED1 and

1015 ± 4 Ma (n = 12, MSWD = 1.11) for the OLT1, respectively. Every six analyses were followed by two analyses of the standard sphene MKED1 and two analyses of the standard sphene OLT1. Isotopic ratios were calculated using ICPMSDataCal 8.4 [55] and were plotted using Isoplot version 3.0 software [56]. Common Pb corrections were made using the method of [57].

3.2. Whole-Rock Major and Trace Elements Analysis

After the removal the altered surfaces, fresh samples were selected, crushed and powdered to less than 200 mesh in an agate mill for whole-rock analysis. Briefly, 1 g of sample was weighed and put into the crucible and baked in a high temperature furnace at 1000 °C for 1h to obtain the loss on ignition (LOI). Major elements were analyzed by X-ray fluorescence using a Axios PW4400 spectrometer at the testing center of Shandong Provincial Lunan Geology and Exploration Institute, China. Trace elements were determined using a Anglient 7900 ICP-MS instruments with analytical uncertainties of 1–3%. Details of the analytical techniques are described by [58]. Analyses of basalt and andesite standards (BHVO-1, BCR-2 and AGV-1) indicated that the analytical precision and accuracy were better than 5% for major elements and 10% for trace elements and REEs.

4. Results

4.1. Petrology and Rock Association

The Longbaoshan alkaline complex is the host rock of the Longbaoshan rare earth element deposit. The alkaline complex includes the hornblende diorite, hornblende syenite porphyry, biotite monzonite porphyry and aegirine diorite porphyrite (Figure 1c) [44]. Among them, the hornblende diorite exposes in the northwest area of Longbaoshan and hornblende syenite porphyry, biotite monzonite porphyry and aegirine diorite porphyrite are exposed in the southeast area of Longbaoshan.

4.1.1. Hornblende Diorite

Hornblende diorites (21LBS27-1 to 21LBS27-5, 35°02′02″ N, 117°45′54″ E) show light brown to greenish color and granular texture. The rocks are fine grained and mainly composed of plagioclase (60–65 vol.%), amphibole (27–32 vol.%) and small amounts of quartz (3–5 vol.%) and biotite (2–4 vol.%) (Figure 2a). Accessory minerals include apatite, sphene and zircon. Amphibole is subhedral to anhedral with grain sizes of 150–400 μm. Plagioclase show grain size of 250–350 μm and typical polysynthetic twinning (Figure 3a,b). The plagioclase shows carlsbad and polysynthetic twining, which are analogous to the albite and oligoclase, respectively.

4.1.2. Hornblende Syenite Porphyry

The hornblende syenite porphyries (21LBS28-1 to 21LBS28-4, 35°00′32″ N, 117°46′55″ E) are light pink colored with a porphyritic texture (Figure 2b). The phenocryst is composed of plagioclase (20–25 vol.%) and hornblende (5–7 vol.%). The matrix is mainly composed of orthoclase (30 vol.%) and plagioclase (35 vol.%). The accessory minerals are apatite and zircon. Plagioclase phenocrysts are euhedral with grain sizes of 500–3000 μm. Their polysynthetic twinning indicates an albite composition. Hornblende is euhedral with grain sizes of 500–1000 μm (Figure 3c,d).

4.1.3. Biotite Monzonite Porphyry

Biotite monzonite porphyries (21LBS29-1 to 21LBS29-4, 35°00′10 N, 117°46′22 E) are medium-to-coarse grained, with porphyry texture, which is dominated by orthoclase (50–55 vol.%), plagioclase (35–40 vol.%) and biotite (5–10 vol.%) (Figure 2c). Accessory minerals in these rocks are mainly composed of apatite and zircon. The phenocrysts are composed of plagioclase and orthoclase. Plagioclase phenocryst shows euhedral morphology with a grain size of 0.5–1.0 cm. The polysynthetic twinning with locally zoning texture is developed in the plagioclase, which is analogous to the oligoclase. Orthoclase is euhedral

to subhedral with a grain size of 300–500 μm and typical Carlsbad twinning (Figure 3e,f). The biotite shows a brownish color, indicating high iron and titanium contents. The matrix is cryptocrystalline and composed of plagioclase, orthoclase and biotite.

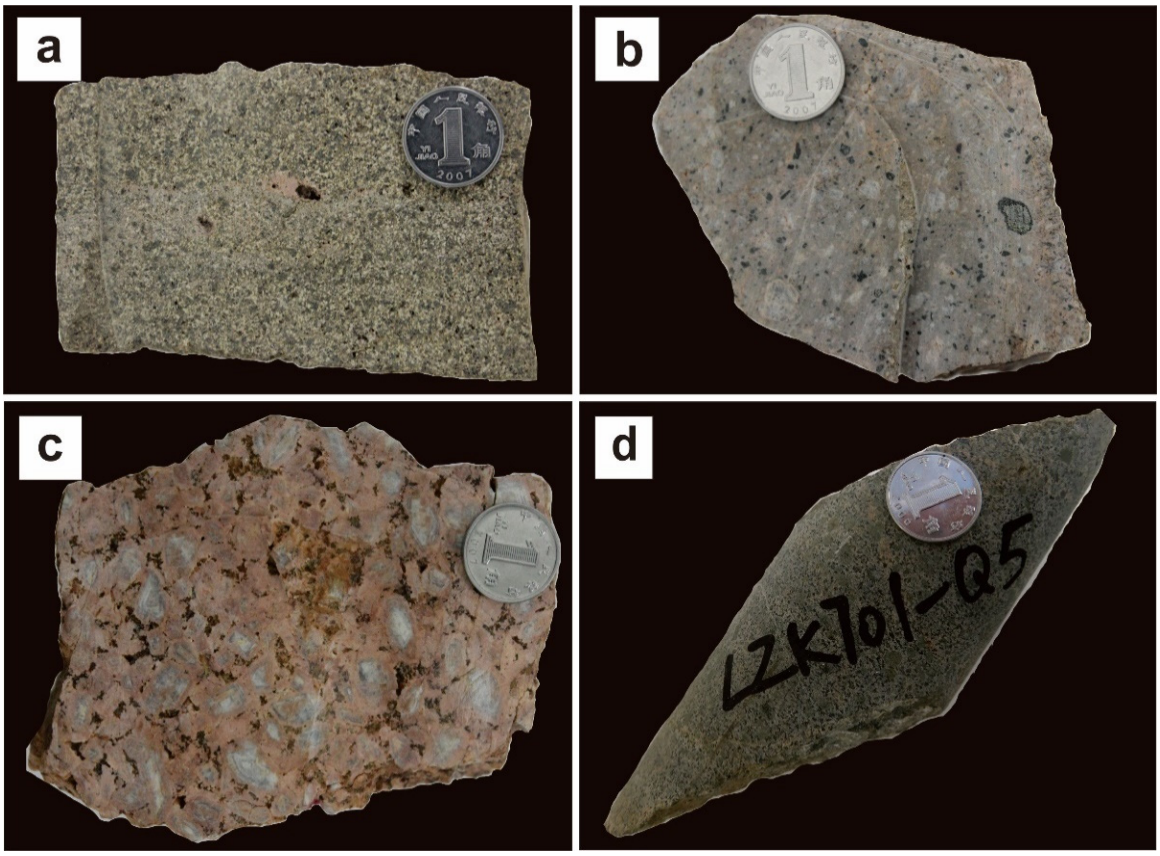

Figure 2. Photographs of alkaline complex from the Longbaoshan area. (**a**) Hornblende diorite. (**b**) Hornblende syenite porphyry. (**c**) Biotite monzonite porphyry. (**d**) Aegirine diorite porphyrite.

4.1.4. Aegirine Diorite Porphyrite

Aegirine diorite porphyrites (21LBS30-1 to 21LBS30-2, 35°00′43″ N, 117°47′09″ E) show dark green or gray color, porphyritic texture and massive structure (Figure 2d). The aegirine diorite porphyrite dominantly consists of K-feldspar (55–60 vol.%), aegirine pyroxene (15–20 vol.%), amphibole (15–20 vol.%), biotite (5–10 vol.%). Accessory minerals include zircon, monazite and apatite. Aegirine pyroxene and amphibole are light to dark green, which dominate the phenocrysts of these rocks. Aegirine pyroxenes show medium grain sizes of 1500–2000 μm and orange to blue interference color. Amphiboles are coarse grained and the grain size is 2000–3500 μm. Biotite is brown in color with grain sizes of 1000–1500 μm, which means a high content of titanium (Figure 3g,h).

4.2. Geochronology and REE Geochemistry of Sphene

The sphene grains from the hornblende diorite (21LBS27) are euhedral to subhedral and range from 70 to 200 μm in size, with length-to-width ratios of 1:1 to 2.5:1. Most of the sphenes show oscillatory zoning in the CL images. Twenty-nine sphene grains were selected for U-Pb analysis. The analyzed spots yield lower intercept age of 120 ± 8.2 Ma on a Tera–Wasserburg diagram (2σ, n = 29, MSWD = 2.4) (Figure 4). They show Th and U contents of 193 to 533 ppm and 28 to 98 ppm, respectively. The Th/U ratios are high and range from 5.0 to 11.2 (Table 1).

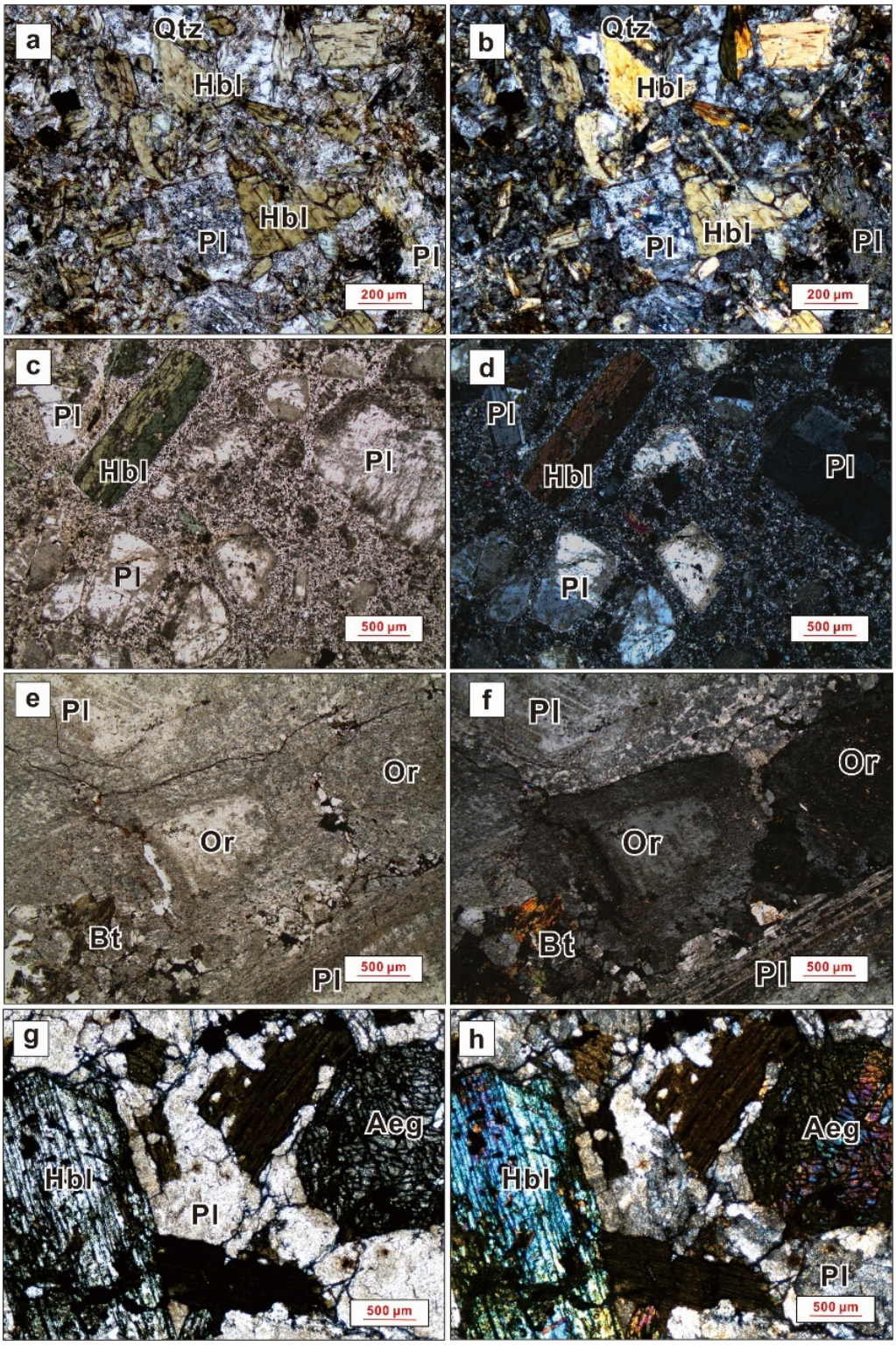

Figure 3. Photomicrographs showing characteristics of alkaline complex from Longbaoshan area. (**a**,**b**) Hornblende diorite. (**c**,**d**) Hornblende syenite porphyry. (**e**,**f**) Biotite monzonite porphyry. (**g**,**h**) Aegirine diorite porphyrite. Pl—plagioclase; Or—orthoclase; Hbl—hornblende; Qtz—quartz; Aeg—Aegirine pyroxene. The left column includes crossed-polarized light photomicrographs and the right column includes plane-polarized light photomicrographs.

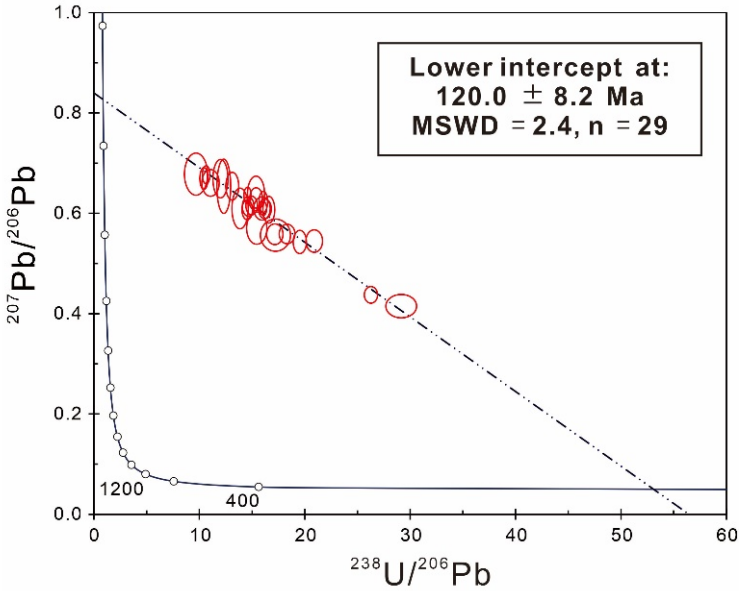

Figure 4. Sphene U-Pb lower intercept ages of the hornblende diorite (21LBS27) from the Longbaoshan alkaline complex.

Table 1. LA-ICP-MS sphene U-Pb isotope data of hornblende diorite.

Sample No.	Th (ppm)	U (ppm)	Th/U	Isotopic Ratios					
				$^{207}Pb/^{206}Pb$		$^{207}Pb/^{235}U$		$^{206}Pb/^{238}U$	
				Ratio	1σ	Ratio	1σ	Ratio	1σ
21LBS27-1-1	358	39.5	9.05	0.6090	0.0080	5.1845	0.1089	0.0617	0.0010
21LBS27-1-2	365	55.8	6.53	0.6767	0.0074	8.7660	0.1423	0.0940	0.0013
21LBS27-1-3	256	31.2	8.20	0.6397	0.0141	5.6718	0.0875	0.0650	0.0014
21LBS27-1-4	450	54.7	8.23	0.5447	0.0092	3.5756	0.0577	0.0478	0.0007
21LBS27-1-5	499	98.9	5.04	0.4150	0.0095	1.9649	0.0618	0.0343	0.0007
21LBS27-1-6	432	44.5	9.72	0.6229	0.0086	5.3270	0.0581	0.0623	0.0007
21LBS27-1-7	345	30.6	11.27	0.6095	0.0166	6.0363	0.1665	0.0721	0.0017
21LBS27-1-8	308	31.8	9.68	0.6361	0.0065	5.9900	0.0554	0.0686	0.0007
21LBS27-1-9	348	34.9	9.97	0.6137	0.0079	5.7541	0.0854	0.0683	0.0011
21LBS27-1-10	258	28.8	8.96	0.6607	0.0109	8.2779	0.3041	0.0905	0.0028
21LBS27-1-11	315	47.7	6.61	0.5588	0.0079	4.2311	0.1059	0.0546	0.0009
21LBS27-1-12	303	42.4	7.17	0.5704	0.0131	5.0765	0.1669	0.0648	0.0017
21LBS27-1-13	232	40.8	5.69	0.5628	0.0101	5.0545	0.1080	0.0654	0.0012
21LBS27-1-14	251	32.6	7.71	0.6782	0.0172	9.7381	0.5922	0.1033	0.0048
21LBS27-1-15	334	43.4	7.70	0.5564	0.0131	4.5255	0.2200	0.0581	0.0020
21LBS27-1-16	304	35.5	8.57	0.5448	0.0104	4.5233	0.1461	0.0603	0.0018
21LBS27-1-17	258	33.9	7.61	0.6541	0.0112	6.8752	0.1406	0.0762	0.0015
21LBS27-1-18	249	29.6	8.40	0.6695	0.0089	8.8449	0.1527	0.0959	0.0014
21LBS27-1-19	290	33.1	8.76	0.6540	0.0221	7.2784	0.2082	0.0812	0.0017
21LBS27-1-20	297	42.6	6.96	0.6070	0.0081	5.7573	0.1128	0.0688	0.0010
21LBS27-1-21	533	78.0	6.84	0.4375	0.0068	2.2837	0.0281	0.0381	0.0004
21LBS27-1-22	298	36.4	8.20	0.6308	0.0083	5.6424	0.0961	0.0650	0.0010
21LBS27-1-23	193	34.8	5.55	0.6691	0.0156	7.6781	0.2354	0.0834	0.0020
21LBS27-1-24	358	50.6	7.07	0.6155	0.0077	5.6589	0.0994	0.0668	0.0010
21LBS27-1-25	372	36.7	10.16	0.6094	0.0056	5.2025	0.0411	0.0622	0.0005
21LBS27-1-26	210	37.6	5.58	0.5583	0.0084	4.4746	0.0954	0.0583	0.0011
21LBS27-1-27	356	47.2	7.56	0.5429	0.0094	3.7715	0.0532	0.0512	0.0007
21LBS27-1-28	275	42.1	6.53	0.6097	0.0094	5.3095	0.1513	0.0628	0.0013
21LBS27-1-29	297	30.8	9.64	0.6071	0.0108	4.9978	0.0711	0.0603	0.0008

Total REE contents of the sphene from the hornblende diorite range from 2.4% to 4.4%. The light rare earth element (LREE) content ranges from 2.4% to 4.1%, and that of heavy rare earth (HREE) is 0.16–0.18% (Figure 5). The chondrite normalized patterns of the sphene are right inclined, with LREE/HREE (without normalization) and $(La/Yb)_N$ (normalized to chondrite) ratios ranging from 16 to 42 and 33 to 75, respectively. LREE enrichment and HREE depletion are obvious. Most of the sphenes exhibit weak negative Eu anomalies (n = 26, 0.44–0.89) and a few sphenes exhibit weak positive Eu anomalies (n = 3, 1.07–1.65). All sphenes show positive Ce anomalies (mostly 1.21–1.37) (Table 2).

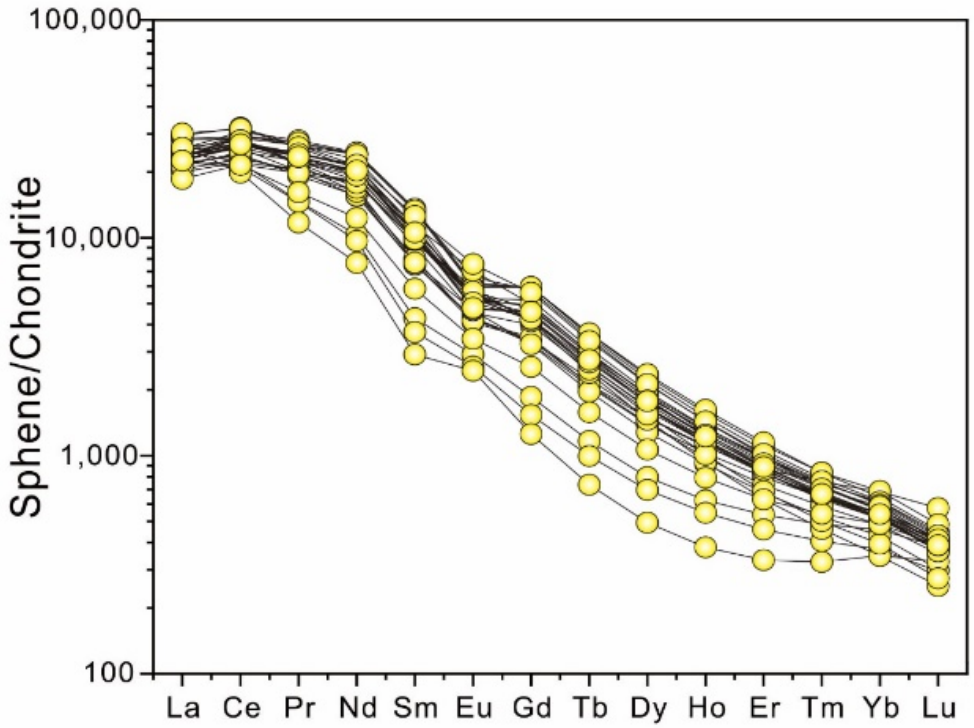

Figure 5. Chondrite-normalized REE patterns of sphene from the hornblende diorite (21LBS27) of the Longbaoshan alkaline complex. Chondrite values are from [59].

4.3. Whole-Rock Major and Trace Elements Geochemistry

Given the loss on ignition (LOI) values for most of the analyzed samples, major element concentrations were recalculated on an anhydrous basis.

Major element results indicate that the hornblende diorites show high concentrations of SiO_2 (55.5–57.8 wt.%), MgO (8.4–9.7 wt.%), Fe_2O_3 (8.7–10.0 wt.%), Al_2O_3 (10.8–11.7 wt.%) and CaO (3.5–5.1 wt.%) and low concentrations of Na_2O (1.8–3.3 wt.%) and K_2O (1.5–2.2 wt.%) (Table 3). These rocks show total alkali ($K_2O + Na_2O$) contents of 3.6–5.0 wt.% and are corresponding to gabbro diorite and diorite compositions (Figure 6a). In terms of the alumina saturation index, they are metaluminous (molar ratio $Al_2O_3/(CaO+Na_2O+K_2O)$ (A/CNK): 0.7–0.8; molar ratio $Al_2O_3/(Na_2O+K_2O)$ (A/NK): 1.5–2.2) (Figure 6b)). These samples also exhibit high K_2O/Na_2O ratios (0.5–1.1), which, together with the high K_2O abundance, indicate that the hornblende diorites belong to the medium-to-high K calc-alkaline series (Figure 6c,d).

The hornblende syenite porphyries and biotite monzonite porphyries show a higher concentration of SiO_2 (64.0–68.8 wt.%), Na_2O (5.7–6.5 wt.%), K_2O (3.2–5.0 wt.%) and Al_2O_3 (14.2–17.6 wt.%) and lower concentrations of CaO (0.6–3.1 wt.%), MgO (0.2–1.8 wt.%) and Fe_2O_3 (2.1–4.8 wt.%) than the hornblende diorites (Table 3). The analyzed data of these samples exhibit high contents of total alkali (8.8–11.1 wt.%) and plot into the monzonite, syenite and quartz monzonite fields in the TAS diagram (Figure 6a). The low aluminum saturation index of A/CNK (0.7–0.9) and A/NK (0.9–1.1) suggest that these rocks belong to

the metaluminous and peralkaline series (Figure 6b). The high K_2O/Na_2O (0.6–0.8) ratios and K_2O abundance indicate that these rocks have high-K calcic-alkaline and shoshonite affinities (Figure 6c,d).

Table 2. REE compositions for the sphene in the alkaline complex of the Longbaoshan area (ppm). Ce * : theoretical Ce value, Eu * : theoretical Eu value.

Spot	La	Ce	Pr	Nd	Sm	Eu	Gd	Tb	Dy	Ho	Er	Tm	Yb	Lu	Ce/Ce *	Eu/Eu *
21LBS27-1-1	5956	16,565	2134	8535	1401	262.3	817.9	92.11	408.2	64.80	138.2	16.52	89.62	9.79	1.30	0.56
21LBS27-1-2	4871	14,135	1937	8332	1479	306.9	867.1	96.60	424.2	66.96	141.8	16.96	92.71	10.35	1.27	0.69
21LBS27-1-3	5395	15,888	2134	8898	1519	306.5	856.4	96.51	419.5	64.78	138.2	16.33	88.58	9.49	1.32	0.67
21LBS27-1-4	5948	13,558	1397	4818	654	168.9	382.4	43.63	202.3	35.35	88.7	12.34	77.81	9.69	1.33	1.07
21LBS27-1-5	5691	15,796	1921	7251	1162	248.6	695.5	79.59	378.4	62.16	144.1	19.35	116.05	14.61	1.37	0.72
21LBS27-1-6	6684	17,314	2048	7523	1148	247.5	674.3	77.54	354.5	58.16	132.0	16.39	92.80	10.14	1.32	0.74
21LBS27-1-7	5897	18,054	2519	10,673	1848	305.5	1068.5	116.23	500.8	76.48	160.9	18.23	95.23	10.61	1.32	0.44
21LBS27-1-8	5524	17,565	2518	11,231	2025	383.3	1180.6	129.13	545.4	81.28	165.3	18.56	96.36	10.08	1.33	0.57
21LBS27-1-9	6973	19,565	2526	9982	1638	330.6	965.8	108.82	488.0	75.74	164.3	19.20	102.68	10.72	1.31	0.65
21LBS27-1-10	5571	18,046	2601	11,342	2035	351.8	1220.1	135.84	587.8	88.89	184.7	21.35	109.61	11.50	1.35	0.47
21LBS27-1-11	6071	18,769	2654	11,503	2079	358.3	1218.3	132.62	567.3	85.03	175.4	20.01	105.58	11.26	1.31	0.47
21LBS27-1-12	5625	16,727	2330	9970	1722	307.9	988.5	107.82	463.7	69.50	144.2	16.56	86.57	9.54	1.28	0.52
21LBS27-1-13	5319	16,236	2237	9397	1607	305.1	923.0	101.02	440.4	67.27	138.2	16.03	87.58	9.26	1.33	0.59
21LBS27-1-14	5214	14,711	1832	7284	1169	237.4	700.4	84.03	381.0	63.05	137.2	16.66	91.71	9.86	1.36	0.64
21LBS27-1-15	5418	16,351	2304	9863	1724	300.4	1011.0	110.86	479.7	73.36	155.6	18.30	96.31	10.52	1.29	0.48
21LBS27-1-16	5230	14,564	1886	7604	1226	241.4	718.6	79.07	358.4	55.24	121.5	14.95	81.83	9.00	1.29	0.62
21LBS27-1-17	5534	17,946	2596	11,214	2040	344.5	1223.0	136.50	601.1	91.90	190.3	21.34	117.01	12.31	1.35	0.44
21LBS27-1-18	6879	17,443	2100	7900	1176	269.1	666.6	73.52	325.5	52.07	111.9	13.39	72.77	7.65	1.27	0.86
21LBS27-1-19	5608	16,755	2247	9276	1581	273.5	934.1	104.75	470.0	74.34	160.1	18.99	104.62	10.95	1.34	0.47
21LBS27-1-20	5280	12,899	1386	4513	565	148.7	315.9	37.28	177.0	30.93	75.9	10.34	63.26	7.47	1.37	1.16
21LBS27-1-21	6232	12,179	1116	3581	445	142.3	258.3	27.53	125.3	21.49	54.9	8.31	59.20	8.29	1.28	1.65
21LBS27-1-22	7140	19,360	2477	9628	1499	322.7	873.2	95.49	424.8	65.42	142.4	16.84	89.40	9.44	1.27	0.74
21LBS27-1-23	4745	13,646	1936	8470	1488	340.1	848.9	89.67	371.4	52.86	104.6	11.77	58.94	6.41	1.22	0.86
21LBS27-1-24	5050	15,153	2140	9323	1736	409.7	1020.0	111.21	482.6	71.66	147.6	17.40	91.28	9.23	1.28	0.89
21LBS27-1-25	5578	16,532	2310	10,104	1926	439.6	1149.4	125.76	541.6	81.36	168.9	19.52	101.30	10.21	1.27	0.82
21LBS27-1-26	4412	13,259	1880	8307	1496	328.3	868.5	92.92	391.8	57.23	113.6	12.77	66.95	6.95	1.27	0.78
21LBS27-1-27	5351	13,208	1535	5757	892	199.4	524.9	59.17	271.0	44.83	104.4	13.79	82.45	9.85	1.28	0.79
21LBS27-1-28	6132	17,146	2226	8984	1505	292.4	872.6	100.07	454.9	70.66	152.5	18.00	99.41	10.48	1.29	0.61
21LBS27-1-29	5351	16,414	2237	9492	1620	276.5	941.0	103.03	452.6	69.33	146.9	17.03	91.73	9.86	1.35	0.47

The major element analysis of the aegirine diorite porphyrites shows a similar composition of SiO_2 (56.6–63.8 wt.%), Na_2O (3.9–5.2 wt.%), K_2O (4.1–4.8 wt.%) and Al_2O_3 (12.7–14.0 wt.%) and higher concentrations of MgO (2.5–3.9 wt.%) and Fe_2O_3 (4.5–6.3 wt.%) compared to the hornblende syenite porphyries and biotite monzonite porphyries (Table 3). The aegirine diorite porphyrites show a high content of total alkali (8.7–9.5 wt.%) and fall into the monzo-diorite and monzonite fields in the TAS diagram (Figure 6a). These rocks are peralkaline and metaluminous (A/CNK is 0.6–0.7; A/NK: 0.9–1.1) (Figure 6b). They show higher K_2O/Na_2O (0.8–1.0) ratios and K_2O contents than the samples described above and fall into high-K calcic-alkaline and shoshonite fields (Figure 6c,d).

The primitive mantle-normalized trace element patterns reflect distinctly negative anomalies of Th, Ce, Nb-Ta and Zr-Hf and positive anomalies of LILE (Pb, Ba, Sr) and La for these rocks (Figure 7a). Chondrite-normalized REE patterns of the samples from the Longbaoshan alkaline complex show LREE enrichment and variable HREE depletion (LREE/HREE = 2.82–34.26) and high values of $(La/Sm)_N$: 3.17–10.06, $(La/Yb)_N$: 18–513 and $(Gd/Yb)_N$: 3.2–47.5, indicating a strong fractionation between LREE and HREE (Figure 7b). The variable enrichment of REE (1 to 1000 times) indicates that the rare earth elements were partitioned among different minerals during fractional crystallization [59].

Table 3. Major (wt.%) and trace elements (ppm) of alkaline rocks from Longbaoshan alkaline complex.

Sample No.	21LBS27-1	21LBS27-2	21LBS27-3	21LBS27-4	21LBS27-5	21LBS28-1	21LBS28-2	21LBS28-3	21LBS29-1	21LBS29-2	21LBS29-3	21LBS29-4	21LBS30-1	21LBS30-2	21LBS30-3
Rock Type	**Hornblende Diorite**					**Hornblende Syenite Porphyry**			**Biotite Monzonite Porphyry**				**Aegirine Diorite porphyrite**		
Major elements (wt. %)															
SiO_2	54.96	55.24	54.49	53.36	54.30	66.9	67.9	63.8	67.3	66.1	67.3	67.6	56.9	61.9	62.4
Al_2O_3	10.51	10.73	10.24	11.20	10.43	14.8	14.1	14.8	16.4	17.5	16.8	16.6	14.1	14.1	12.4
Fe_2O_3	8.73	8.25	9.46	9.15	9.21	3.39	3.33	4.75	2.45	2.91	2.01	2.06	6.35	4.93	4.41
CaO	3.3	3.69	4.17	4.90	4.57	1.96	1.72	3.13	0.57	1.23	0.59	0.61	5.45	4.14	3.55
MgO	8.67	8.52	9.2	8.09	8.80	1.02	1.32	1.81	0.2	0.41	0.14	0.17	3.96	3.09	2.45
K_2O	2.12	1.56	1.78	2.05	1.40	3.48	3.63	3.18	4.55	4.01	4.83	4.6	4.86	4.1	4.14
Na_2O	2.72	3.19	1.67	2.60	2.83	6.48	5.66	5.58	6.29	6	5.98	6.26	3.91	4.88	5.12
FeO	2.94	2.82	2.4	3.23	2.73	0.95	0.88	1.51	0.12	0.85	0.12	0.12	3.39	2.64	2.27
MnO	0.11	0.12	0.12	0.12	0.12	0.06	0.06	0.09	0.02	0.07	0.04	0.01	0.12	0.1	0.15
TiO_2	0.98	0.98	1	1.05	1.09	0.28	0.32	0.46	0.2	0.26	0.2	0.19	0.74	0.63	0.5
P_2O_5	0.32	0.33	0.28	0.34	0.38	0.26	0.33	0.53	0.08	0.11	0.06	0.08	0.73	0.62	0.47
LOI	3.4	3.27	4.16	3.11	3.17	0.5	0.65	0.94	1	1.03	1.11	1.02	1.79	0.66	2.98
Total	98.76	98.69	98.96	99.20	99.02	100.12	99.93	100.56	99.15	100.44	99.25	99.3	102.3	101.75	100.89
A/CNK	0.82	0.79	0.84	0.73	0.72	0.82	0.86	0.81	1.01	1.06	1.04	1.01	0.65	0.7	0.64
A/NK	1.55	1.55	2.19	1.72	1.69	1.03	1.07	1.17	1.07	1.23	1.12	1.09	1.21	1.13	0.96
Trace elements (ppm)															
Be	1.26	1.12	1.06	0.98	1.12	2.96	2.17	3.04	2.91	2.37	3.15	2.49	3.56	3.49	7.25
Sc	13	13.2	15.8	17.6	12.6	0.54	0.44	0.71	0.87	0.29	0.58	0.63	8.45	5.78	6.49
V	179	175	198	202	185	53.8	68.8	106	38	52.7	32	30.7	143	132	104
Cr	205	277	327	259	251	14.4	8.82	10.7	2.97	5.28	2.16	2.41	60.8	30.9	18.6
Co	35.6	32.9	40.7	39.5	38.5	6.2	7.16	12.8	0.74	5.35	3.22	0.87	19.8	17.8	16.6
Ni	262	247	339	298	295	15.2	8.03	10.1	1.38	3.32	2.7	2.04	39.2	19.2	15.7
Cu	57.7	56.8	28.2	41.5	58.6	38.8	82.8	34.6	20.1	10.4	7.09	26.8	31.7	96.4	268
Zn	119	75.1	82.9	88.2	114	41.8	64.5	102	81.4	103	93.7	79.6	145	138	203
Ga	22.4	23.6	21	21.1	22.4	41.6	38.4	50.4	48	50.8	38.5	47.2	33.9	33.5	34
Rb	63.6	46.7	50.4	67.2	39.7	82.2	92.8	89.3	134	97.5	132	125	154	117	175
Sr	460	558	599	707	856	2234	2483	3216	1981	3350	2348	2262	2008	2499	1349
Y	28.9	18.8	16.5	19	16.8	17.1	14.1	23.8	17.3	14.7	12	12.6	22.4	21.1	25.8
Zr	210	176	167	163	170	210	173	356	162	124	188	150	346	443	298
Nb	5.68	7.46	6.06	6.7	5.59	11.5	11.2	13.5	22.3	22.9	20.3	16.8	1.6	0.45	12.8

Table 3. *Cont.*

Sample No.	21LBS27-1	21LBS27-2	21LBS27-3	21LBS27-4	21LBS27-5	21LBS28-1	21LBS28-2	21LBS28-3	21LBS29-1	21LBS29-2	21LBS29-3	21LBS29-4	21LBS30-1	21LBS30-2	21LBS30-3
Rock Type	**Hornblende Diorite**					**Hornblende Syenite Porphyry**			**Biotite Monzonite Porphyry**				**Aegirine Diorite porphyrite**		
Cs	0.52	0.33	0.5	0.44	0.29	0.39	0.47	1.22	0.99	0.93	0.85	0.91	4.55	1.97	2.59
Ba	558	432	613	569	504	2586	3675	4328	4620	3818	6445	4598	2835	3107	2420
La	32	40	31.7	36.5	30.7	265	220	230	201	364	73	212	168	160	197
Ce	60.5	80.7	60.1	70.8	63.4	460	388	502	405	592	152	396	357	332	360
Pr	8.1	9.82	7.69	8.94	7.9	47.8	40.9	53.4	42.6	67.8	17.8	40.4	42.1	38.5	39.9
Nd	32.1	38.1	30	35.7	32	157	135	184	137	215	65.5	128	139	129	129
Sm	6.51	6.57	5.3	6.57	5.79	17.6	15.9	22.6	16.2	23.4	8.56	13.8	19.1	17	16.7
Eu	1.48	2.04	1.66	2.01	1.83	4.51	4.17	5.65	4.11	5.6	2.6	3.7	4.83	4.57	4.31
Gd	7.19	6.37	4.96	6.22	5.49	12.7	10.9	15.1	10.8	14.5	5.92	9.22	13.6	12.2	12.7
Tb	1.12	0.79	0.63	0.77	0.69	1.1	0.99	1.43	1.05	1.28	0.6	0.84	1.31	1.15	1.23
Dy	6.49	4.47	3.6	4.55	3.99	4.53	3.97	6.05	4.36	4.79	2.7	3.39	5.51	5.13	5.53
Ho	0.97	0.64	0.53	0.66	0.57	0.52	0.45	0.78	0.52	0.48	0.31	0.38	0.85	0.76	0.83
Er	2.81	1.99	1.63	2.05	1.8	1.33	1.02	1.94	1.32	1.02	0.88	1.01	2	1.8	2.07
Tm	0.27	0.19	0.15	0.2	0.16	0.07	0.04	0.14	0.09	0.04	0.05	0.06	0.26	0.22	0.24
Yb	1.84	1.37	1.2	1.48	1.23	0.44	0.31	0.82	0.81	0.25	0.51	0.5	1.23	1.15	1.28
Lu	0.18	0.15	0.12	0.17	0.12	0.02	0.01	0.06	0.07	0.01	0.03	0.04	0.21	0.18	0.18
Hf	4.05	3.77	3.47	3.51	3.37	4.58	3.79	6.3	3.04	3.75	3.47	2.75	2.71	3.36	2.93
Ta	0.29	0.42	0.35	0.37	0.32	0.14	0.2	0.29	0.7	0.75	0.49	0.43	0.44	0.43	0.37
Tl	0.26	0.23	0.23	0.24	0.17	0.19	0.25	0.21	0.39	0.35	0.44	0.39	0.59	0.49	0.56
Pb	8.38	8.24	3.88	3.14	5.39	13.7	18.4	28.8	80.2	42.9	41.5	93.5	38.7	34.8	74.3
Th	4.41	4.01	3.79	3.5	2.87	7.43	8.55	8.15	11.1	13.9	5.84	6.98	17	30	25
U	0.92	0.66	0.67	0.62	0.81	2.8	3.84	4.7	6.08	3.66	5.68	5.18	2.7	2.55	4.04

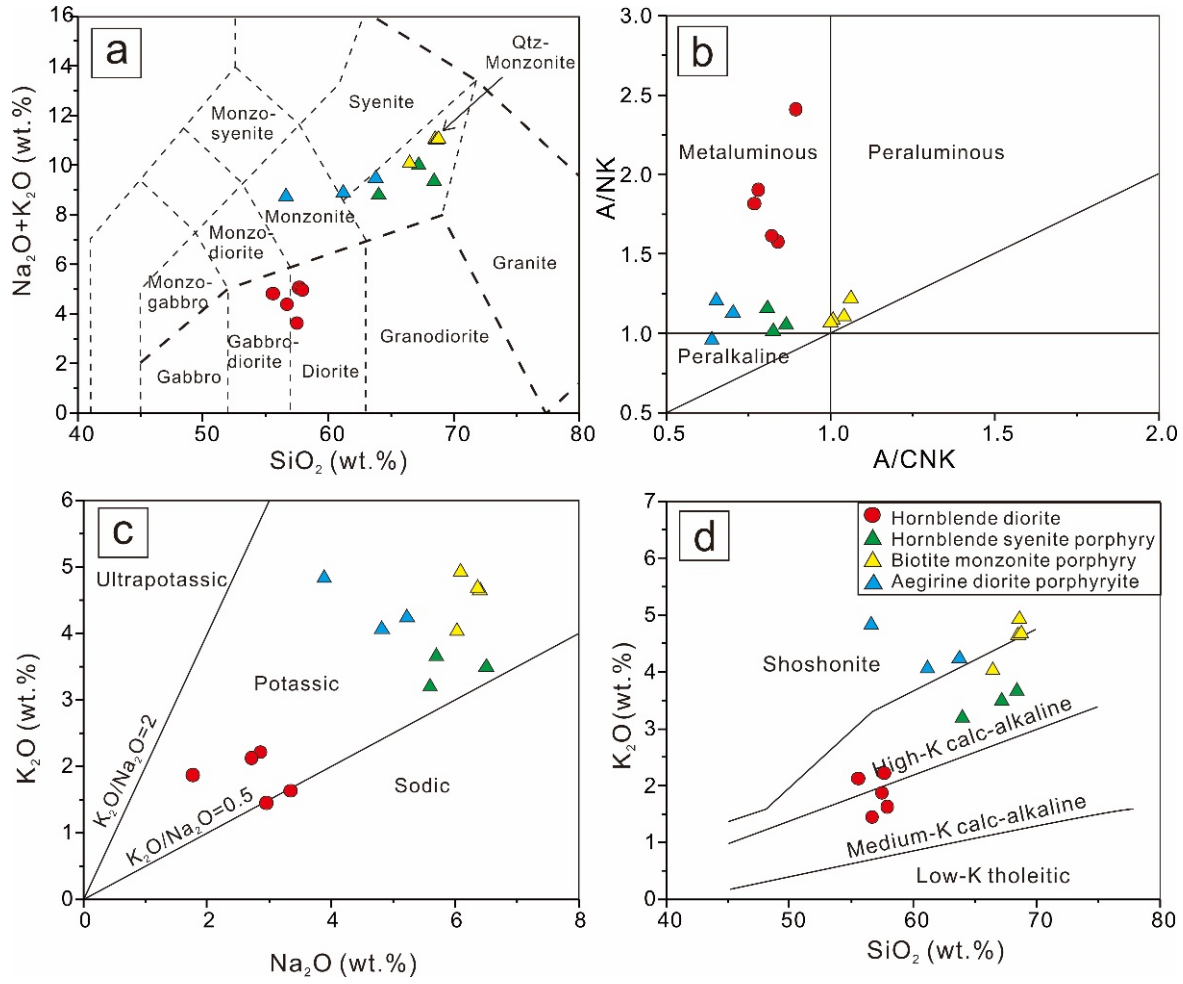

Figure 6. Geochemical diagrams of the alkaline complex in the Longbaoshan area. (**a**) TAS diagram, modified after [60]. (**b**) A/CNK versus A/NK. (**c**) Na_2O versus K_2O, modified after [61]. (**d**) SiO_2 versus K_2O, modified after [62].

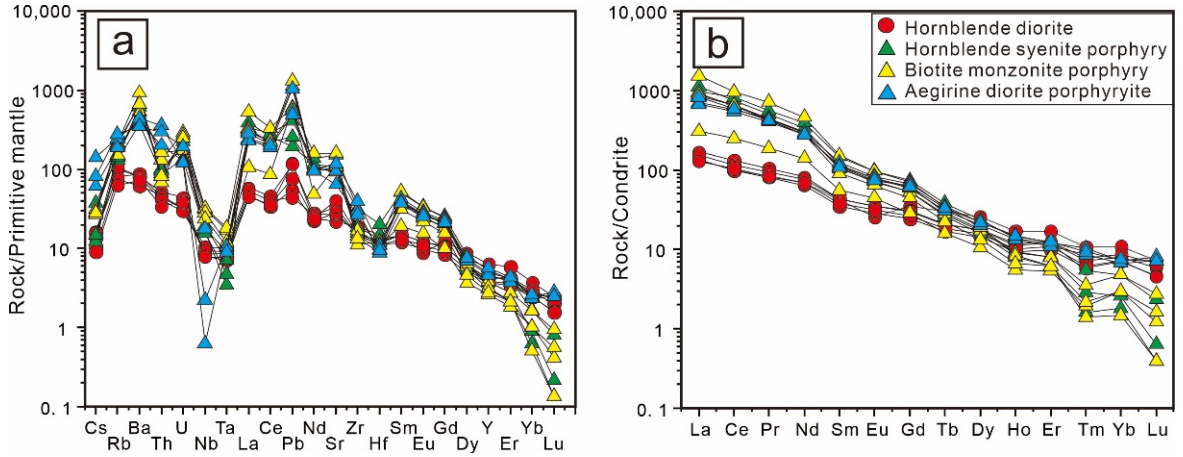

Figure 7. (**a**) Primitive mantle-normalized trace element patterns for the alkaline rocks of the Longbaoshan alkaline complex, modified after [48]. (**b**) Chondrite-normalized REE patterns for the alkaline rocks of the Longbaoshan alkaline complex, with chondrite and PM values from [59].

5. Discussion

5.1. Early Cretaceous Alkaline Granite Magmatism

The eastern North China Craton experienced three peak periods of magmatism during the Mesozoic, which were in the Triassic (216–224 Ma), Jurassic (160–176 Ma) and Early Cretaceous (120–136 Ma) [63]. Lan et al. [33] performed zircon LA-ICP-MS U-Pb dating from the quartz syenite, aegirine-augite syenite, hornblende syenite, monzonite and syenodiorite of the Longbaoshan alkaline complex and suggested that the parent magma was emplaced at 130–129 Ma. Zhou et al. [64] conducted zircon SHRIMP U-Pb dating on the quartz syenite of the Longbaoshan alkaline complex and obtained an age of 125 ± 2.2 Ma. The rare earth element patterns of the sphenes from the hornblende diorite of this study show right-inclined characteristics. And most of sphenes show weak negative Eu anomaly (<1.0) and slight positive Ce anomaly (1.2–1.4) with high Th/U ratio of 1.2–2.3 (Figure 5), which indicates that the sphenes have a magmatic origin. Thus, the sphene U-Pb dating of the 120 ± 8.2 Ma represents the crystallization age of the parent magma of the hornblende diorite. Consequently, the magma emplacement of the Longbaoshan alkaline complex can be constrained at 128–112 Ma, which is consistent with the Early Cretaceous magmatic event in the North China Craton [63].

5.2. The Role of Fractional Crystallization and Assimilation

The formation of the alkaline rock is generally influenced by the magma source, fractional crystallization, accumulation with or without crustal assimilation [8,10,65–68]. The alkaline complex exposed in the Longbaoshan area shows an absence of vertical zoning, namely the ultramafic rock, gabbro, plagioclase, diorite and granite from bottom to top. In addition, the rocks from the Longbaoshan alkaline complex show a porphyry texture and contain phenocrysts without lineation. Consequently, we suggest that cumulation can be excluded in the formation of these rocks.

The negative correlation between SiO_2 and MgO, Fe_2O_3, CaO, Cr and Ni of the samples from the Longbaoshan alkaline complex reflects the removal of pyroxene and amphibole in the early stage of crystallization (Figures 8 and 9). Their low abundance of TiO_2 and the negative correlation of TiO_2 and CaO versus SiO_2 are explained by the crystallization of sphene (Figure 8f). The negative correlation of P_2O_5 and CaO versus SiO_2 of these rocks indicates the crystallization of apatite (Figure 8g). The Zr abundance shows a decreasing trend with the increasing SiO_2 contents (Figure 9e). This feature is qualitatively explained by the removal of zircon in the late stage of fractionation. The positive Ba and Sr versus SiO_2 of these rocks from the Longbaoshan alkaline complex are interpreted as the fractionation of feldspar [69,70].

Crustal contamination may lead to an increasing trend in K_2O/TiO_2 and K_2O/P_2O_5 ratios [71]. The K_2O/TiO_2 ratios of the studied samples from Longbaoshan alkaline complex range from 1.3–2.1 (hornblende diorites) to 6.5–12.8 (hornblende syenite porphyries and aegirine diorite porphyrite) and then increase to 15.5–25.3 (biotite monzonite porphyries), and the K_2O/P_2O_5 (3.68–79.72) ratios are also variable, which indicates crustal contamination in the formation of the Longbaoshan alkaline complex. The Rb/Nb ratios of the samples from the Longbaoshan alkaline complex vary between 4.3 and 32.2 (mostly 6–7), which are significantly higher than the mantle ratios (0.24–0.89) and close to the crust ratios (5.36–6.55). This is consistent with a crustal contamination hypothesis. In addition, the inherited zircons (2.51–2.64 Ga) from the Early Cretaceous Longbaoshan alkaline complex show a similar age to those of zircons from Late Archean gneisses of the Luxi Terrane [72], which, together with the negative $\varepsilon Hf(t)$ values of −19.2 to −12.8 indicate that an ancient crustal material may have been involved in the parent magma [33]. The Nb/Th ratios of the alkaline rocks range from 0.5 to 2.0 and are consistent with the crustal derived alkaline rocks (~1.1), which substantiates the involvement of crustal material [31–34].

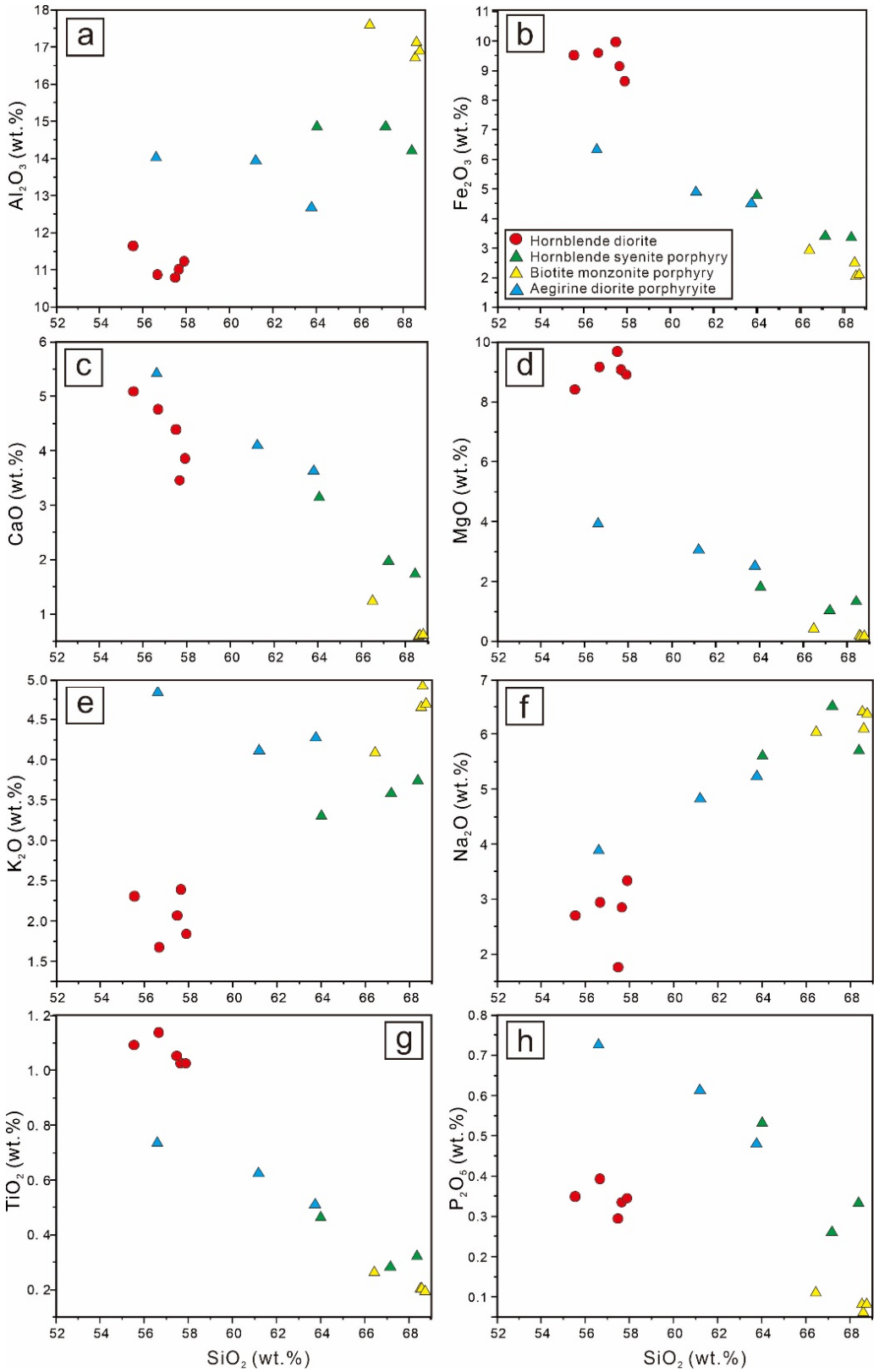

Figure 8. (**a**–**h**) Harker diagrams for major elements of Longbaoshan alkaline complex.

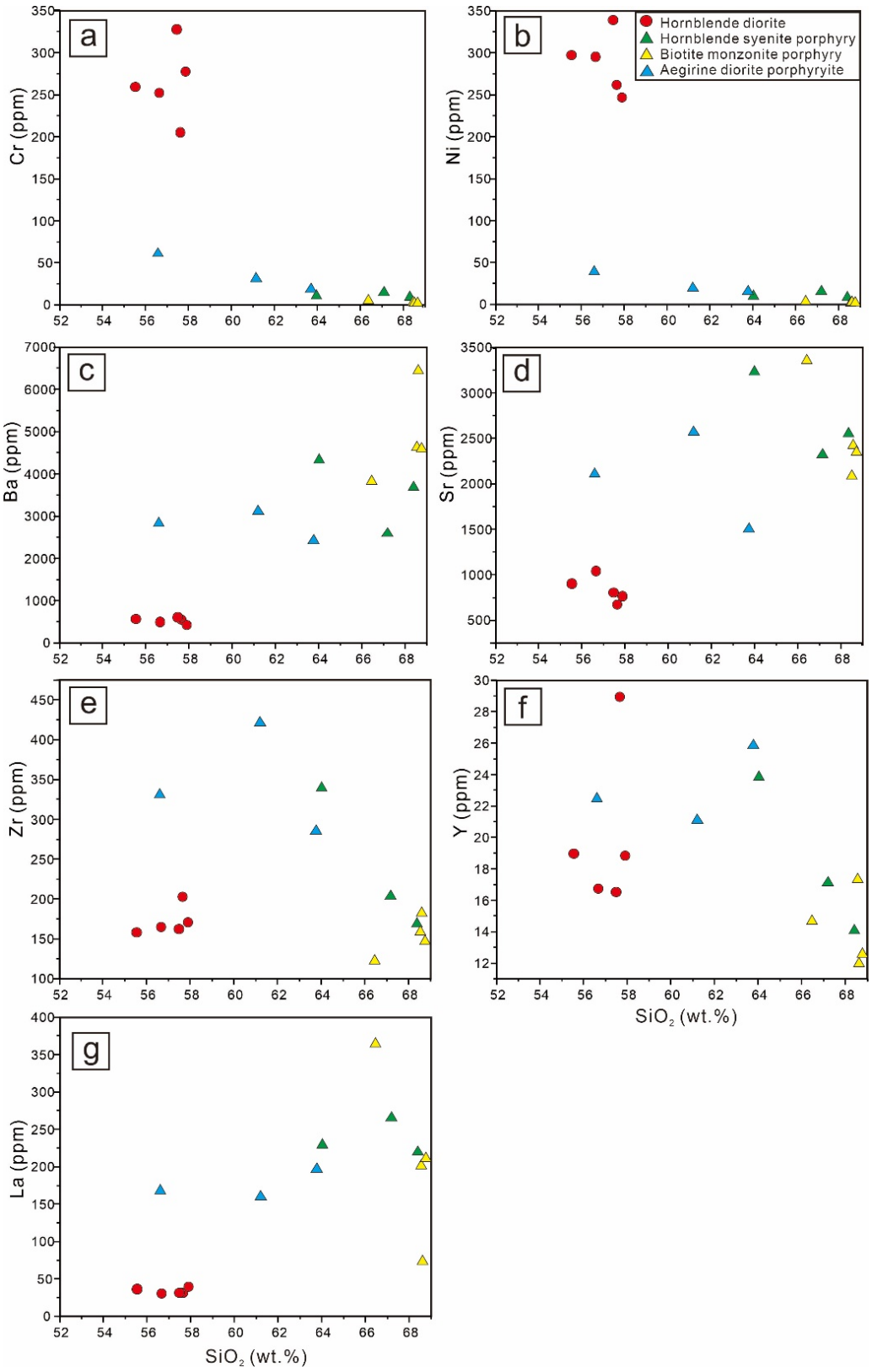

Figure 9. (**a**–**g**) Harker diagrams for trace elements of Longbaoshan alkaline complex.

5.3. Nature of the Alkaline Magma Source

Although the hornblende diorite, hornblende syenite porphyry, biotite monzonite porphyry and aegirine diorite porphyrite from the Longbaoshan alkaline complex show

a diverse composition, their similar ages, whole-rock trace elements patterns suggest that the parent magmas of these rocks were derived from the same magma chamber.

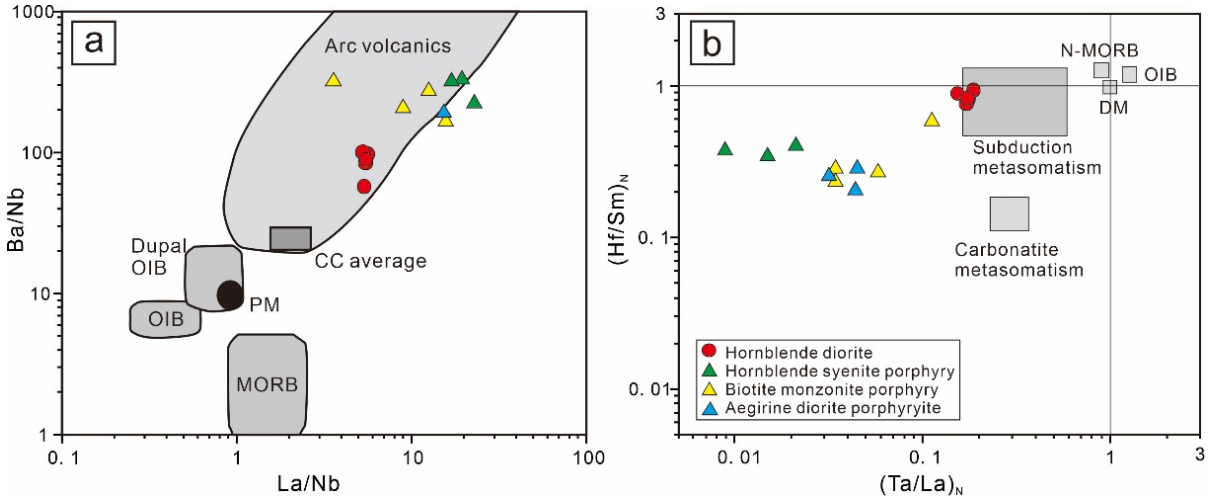

Figure 10. (**a**) Ba/Nb versus La/Nb diagram, modified after [73]. (**b**) $(Ta/La)_N$ versus $(Hf/Sm)_N$ diagram for the Longbaoshan alkaline complex, modified after [74]. CC = continental crust; OIB = ocean island basalts; PM = primitive mantle; MORB = mid-ocean-ridge basalt.

Previous studies have shown that the geochemical composition of the lithospheric mantle of the North China Craton has been changed from a LILE-, Pb- and LREE-enriched and Nb- and Ta-depleted mantle to a LILE- and LREE-enriched mantle with no Nb or even an Nb-enriched and Pb-depleted mantle during the Early Cretaceous [75]. The samples from the Longbaoshan alkaline complex are strongly enriched in LREE and LILE, and depleted in Nb, which together with the high Ba/Nb (218.8) and Rb/Nb (9.5) ratios, indicate that the magma was derived from an enriched mantle source. These features are similar to a subduction-related arc-magmatism-produced rocks [76,77]. In the La/Nb versus Ba/Nb plot, the studied samples from the Longbaoshan alkaline complex fall into the arc volcanics field (Figure 10a), indicating that the mantle source was generated in a subduction zone. The alkaline rocks of the Longbaoshan alkaline complex show a high $(Hf/Sm)_N$ and variable $(Ta/Th)_N$ ratios, indicating a subduction-related metasomatic mantle source region (Figure 10b). The Rb/Sr ratios of the rocks from the Longbaoshan alkaline complex (average 0.07) are lower than the average continent crust (upper crust: 0.31, lower crust: 0.22) and close to the mantle source (0.03), indicating the parent magma was derived from a mantle source [78]. The Ba/Rb ratios of this complex (8-48) are higher than that of the continental crust (8–9), which is consistent with a crustal assimilation mechanism [79]. The Nb/Ta and La/Nb ratios of the samples from this complex are higher than the continental crust (12–13, La/Nb: 1.7) and are consistent with a mantle source (Nb/Ta: 15.5–19.5, La/Nb > 1.7) [78,79]. In addition, the Longbaoshan alkaline complex shows negative εHf(t) values of −19.2 to −13.5 and εNd(t) values of −15.8 to −11.8, which further suggests the mantle source has been enriched [33].

Since the La/Sm and $(La/Yb)_N$ ratios are sensitive to magmatic processes, they can thus be used to determine the role of partial melting and fractional crystallization in the formation of the alkaline complex. The La/Sm and $(La/Yb)_N$ ratios increase with the increase of La contents during partial melting, and the La/Sm and $(La/Yb)_N$ values remain stable with the increase of La contents during fractional crystallization [80]. The alkaline rocks from the Longbaoshan alkaline complex show a positive correlation between La contents and La/Sm, $(La/Yb)_N$ ratios, indicating that partial melting played a significant role in the magma evolution (Figure 11a,b).

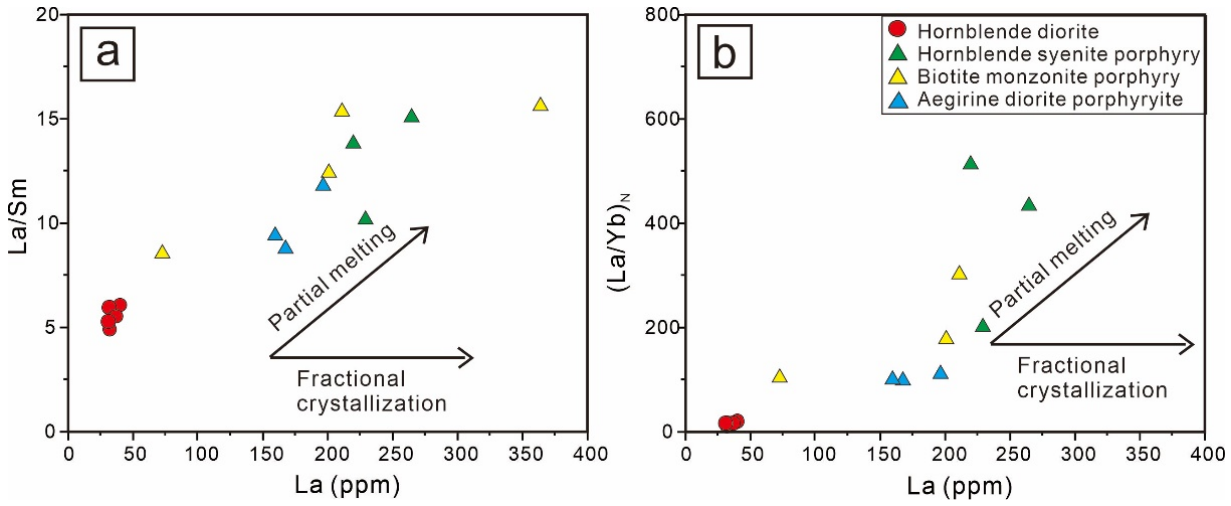

Figure 11. (**a**) La versus La/Sm and (**b**) La versus $(La/Yb)_N$ diagrams for the Longbaoshan alkaline complex showing partial melting and fractional crystallization, modified after [81].

Previous studies suggested that the mantle source can be modified either by dehydration of slab-derived fluids or sediment-derived melts [82,83], which can be distinguished by the incompatible (e.g., Th, Nb, Ta, Ba, Ti and REEs) and compatible elements (e.g., Rb, Sr) [84]. The studied samples show a variable Rb/Y and low Nb/Y ratios, indicating that the mantle source was enriched by sediment-derived melt (Figure 12a). Additionally, the high La/Sm and low Ba/Th ratios (Figure 12b) consistently suggest that an interaction between the mantle source and sediment-derived melts rather than slab-derived fluids. Since high field strength elements (e.g., Nb, Ta) are mainly enriched in the residual rutile and ilmenite phases, the negative anomalies of Nb, Ta and Ti may imply that the occurrence of residual rutile in the mantle source [85,86]. Overall, the magma source of the Longbaoshan alkaline complex was originated from an enriched mantle through partial melting of an enriched mantle leading to the formation of residual rutile, and the mantle source was modified by sediment-derived melt.

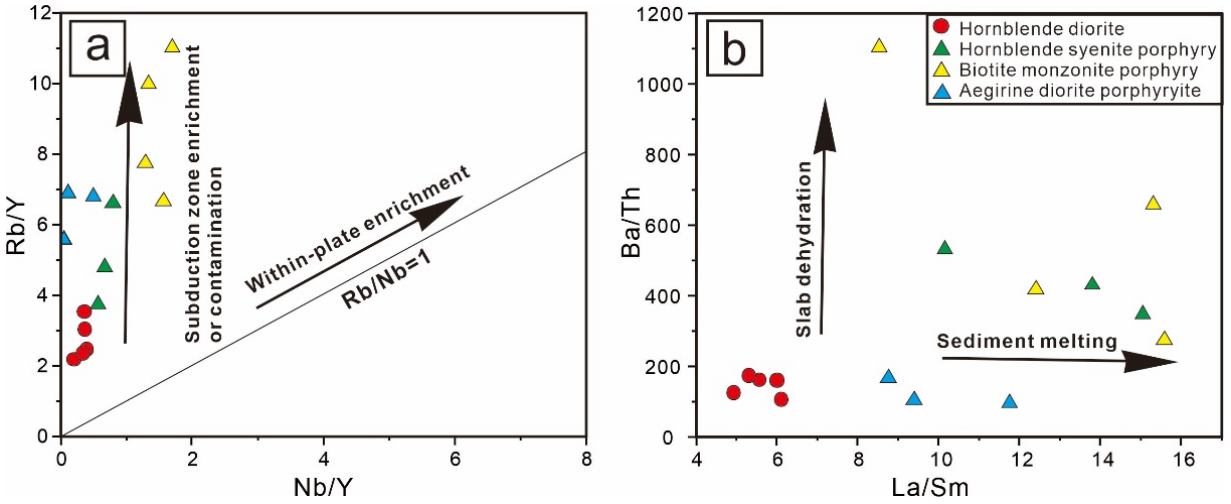

Figure 12. (**a**) Nb/Y versus Rb/Y diagram, modified after [87]. (**b**) La/Sm versus Ba/Th diagram, modified after [87].

5.4. Tectonic Implications

The North China Craton experienced the subduction of the Paleo-Pacific Plate during the Early Jurassic [88–91]. The younging trend magmatism from the west to the east of the

North China Craton suggest a subsequent rollback process of the Paleo-Pacific Plate during the Early Cretaceous [36,92,93], which triggered the upwelling of the asthenosphere, extension and lithospheric thinning as well as associated magmatism [94–97]. In addition, Zhu et al. [98] suggested that the subducting Pacific plate was retreated ca. 880 km during 130–120 Ma. The magma emplacement age of 128–112 Ma of the Longbaoshan alkaline complex is consistent with the timing of the rollback of the Paleo-Pacific Plate (130–120 Ma) [22,94].

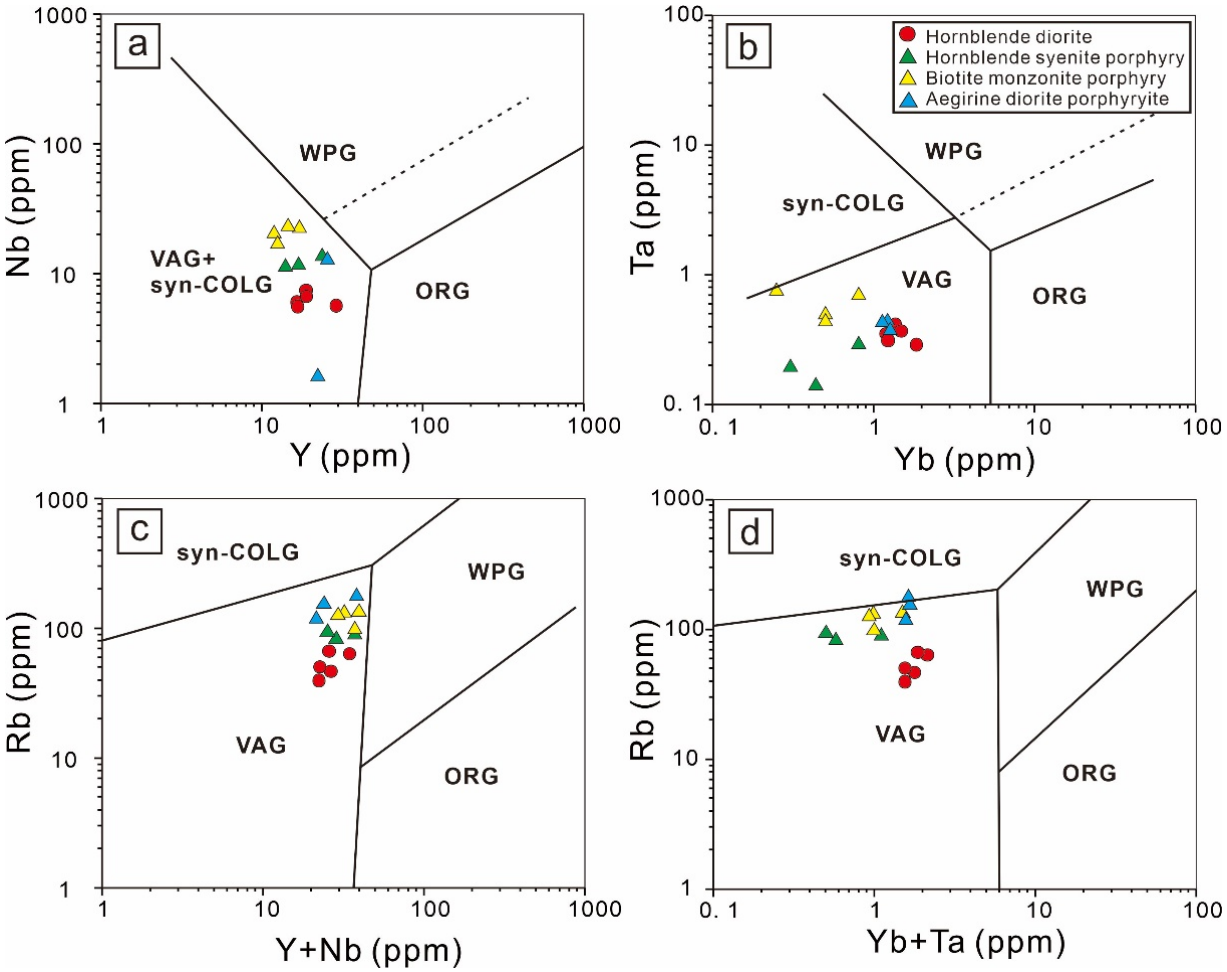

Figure 13. (**a**–**d**) Tectonic discrimination diagrams. (**a**) Nb versus Y diagram, modified after [99]. (**b**) Ta diagram and Yb diagram, modified after [99]. (**c**) Rb versus (Y+Nb) diagram, modified after [99]. (**d**) Rb versus (Yb+Ta) diagram, modified after [99]. VAG = volcanic arc granites, Syn-COLG = syn-collisional granites, WPG = within-plate granites, ORG = ocean-ridge granites.

The alkaline rocks of the Longbaoshan alkaline complex are strongly enriched in LREE and LILEs (e.g., Rb, Ba), and depleted in HREE and HFSEs (e.g., Nb, Ta), which are analogous to volcanic arc granites [100,101]. In the tectonic discrimination diagrams, they are plotted in the volcanic arc granites field, indicating that they were formed in an active continental margin setting (Figure 13a–d). Previous studies have shown that the alkaline magma may be generated from continental arc, post-collisional arc, oceanic arc and within-plate settings [102]. The magma from different tectonic settings shows distinct geochemical features, such as the post-collisional arc magma being characterized by higher ratios of Ce/P and lower ratios of Zr/Ce and Ti/Nb than the continental arc magma and the late oceanic arc magma being characterized by higher concentrations of Hf, La and P than the initial oceanic arc magma [102]. The samples from the Longbaoshan alkaline complex fall within the continental and post-collision arc fields (CAP + PAP) (Figure 14a,b), suggesting

subduction-collision- and post-collision-related settings. In addition, most of these samples plot in the continental arc and minor fall into the post-collisional arc fields (Figure 14c), suggesting that the mantle was enriched in a prior subduction process and the magma was emplaced through a post-collisional extension process. Moreover, in the Nb/Yb versus Th/Yb diagram (Figure 14d), the studied samples fall into the active continental margin field, which further indicates a subduction process [103].

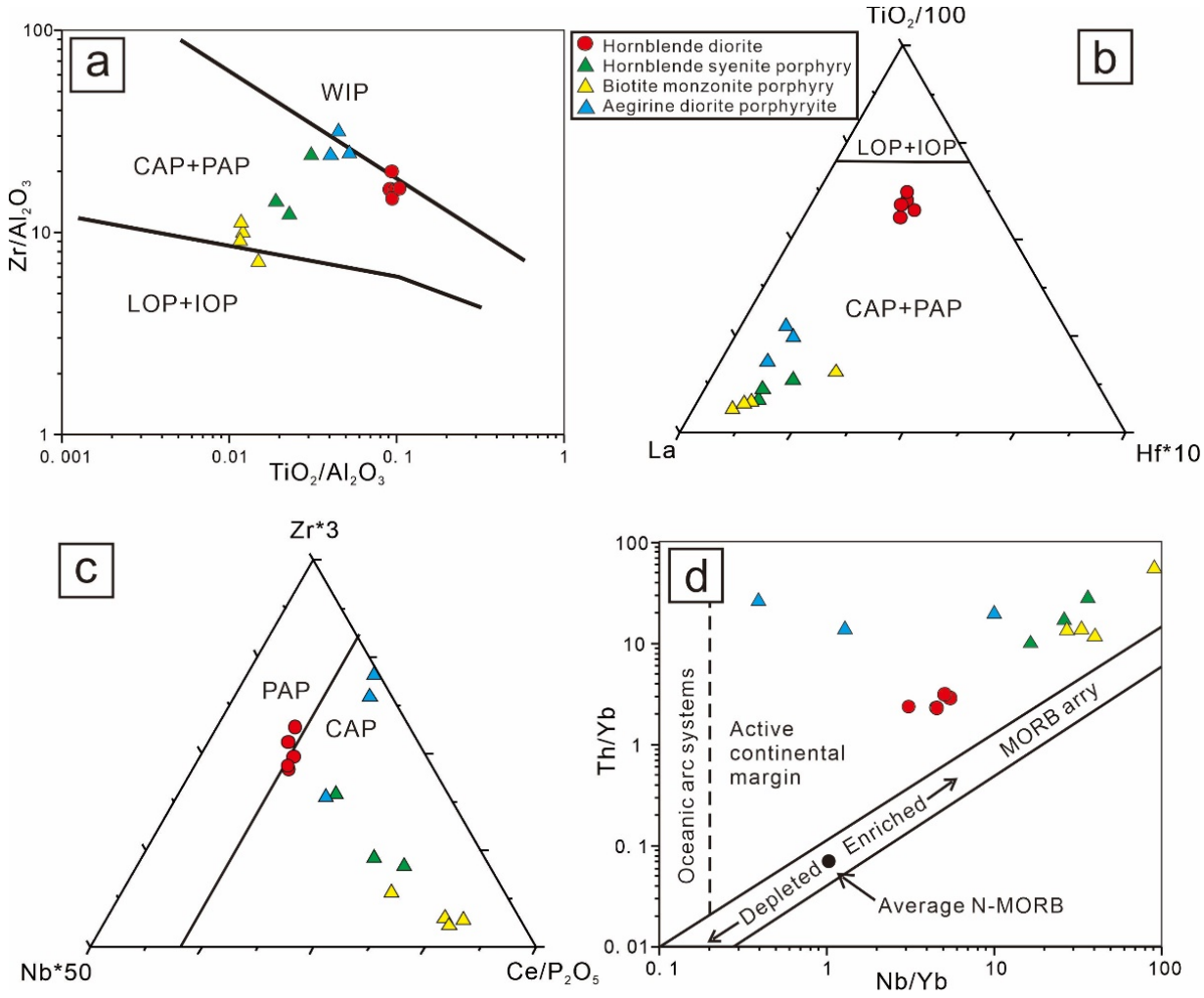

Figure 14. (**a**–**d**) Tectonic discrimination diagrams. (**a**) Zr/Al_2O_3 versus TiO_2/Al_2O_3 diagram, modified after [104]. (**b**,**c**) TiO2-La-Hf diagram and Zr-Nb-Ce/P_2O_5 diagram, modified after [104,105]. (**d**) Nb/Yb versus Th/Yb diagram, modified after [96]. CAP = continental arc potassic rocks; PAP = post-collisional arc potassic rocks; IOP = initial oceanic arc potassic rocks; LOP = late oceanic arc potassic rocks.

In summary, the magma source of the Longbaoshan alkaline complex was originated from a lithospheric mantle which was interacted with sediment-derived melts during a prior subduction process. The magma was emplaced through a subsequent extensional process, which was triggered by the rollback of the subducted plate and upwelling of the asthenosphere [30,96,105]. The parent melts of the Longbaoshan alkaline complex were initially generated by partial melting of an enriched lithospheric mantle, which experienced a subsequent fractional crystallization and assimilation with the continental crust rocks (Figure 15).

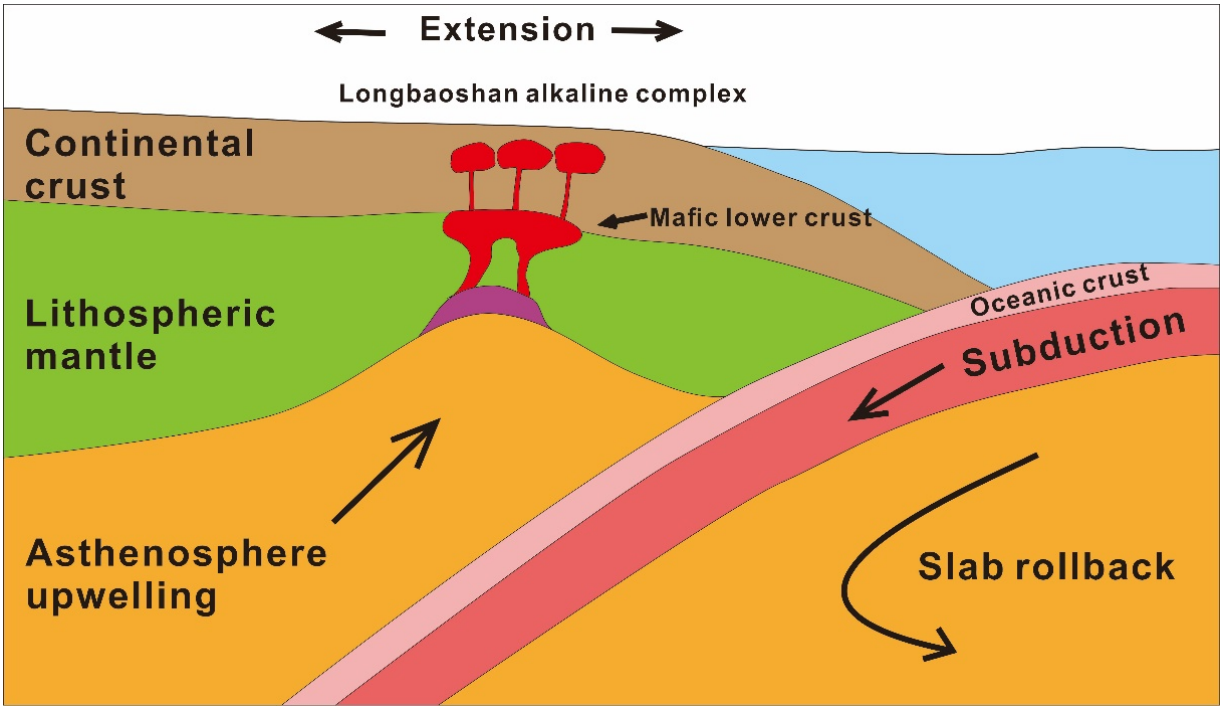

Figure 15. Tectonic schematism showing the formation of the alkaline complex in the Longbaoshan area of Luxi Terrane [40,106,107].

6. Conclusions

(1) The parent magma of the Longbaoshan alkaline complex was crystallized at 128–112 Ma, which is consistent with the Early Cretaceous magmatic event in the North China Craton.
(2) The magma of the Longbaoshan alkaline complex was derived from an enriched lithospheric mantle. The lithospheric mantle was metasomatized by sediment-derived melts during a subduction process.
(3) The parent magma of the Longbaoshan alkaline complex was emplaced in an extensional setting during the rollback of the subducting plate and experienced a subsequent fractional crystallization and continental crust assimilation process.

Author Contributions: Conceptualization: K.-F.Q., H.-C.Y. and M.-G.A.; writing: Z.-Y.Y. and S.-S.L.; review and editing: Z.-Y.Y., H.-C.Y., C.-L.Z., S.-S.L. and Z.S.; formal analysis: Z.-Y.L., H.-C.Y. and J.-Z.G. All authors have read and agreed to the published version of the manuscript.

Funding: This research was funded by the National Natural Science Foundation of China (42203072, 42111530124), the Shandong Provincial Lunan Geology and Exploration Institute (LNY2020-Z02, LNYS202101), the Fundamental Research Funds for the Central Universities (2-9-2021-101), the Innovation and Entrepreneurship Training Program of China University of Geosciences, Beijing (S202111415020), the Beijing Nova Program (Z201100006820097), the 111 Project (BP0719021), the Chinese Postdoctoral Science Foundation (2021M692995), and the 2021 Graduate Innovation Fund Project of China University of Geosciences, Beijing (ZD2021YC040).

Acknowledgments: We thank Sutita Changsing, Gary Liu, Filip Kostic, the Academic Editor and the three anonymous referees for their constructive and insightful comments, which significantly improved this manuscript. We also thank Academician Jun Deng, Deng-Yang He and Ya-Qi Huang for their comments, which greatly helped to improve the manuscript.

Conflicts of Interest: The authors declare no conflict of interest.

References

1. Jung, S.; Mezger, K.; Hoernes, S. Shear zone-related syenites in the Damara belt (Namibia): The role of crustal contamination and source composition. *Contrib. Mineral. Petrol.* **2004**, *148*, 104–121. [CrossRef]
2. Guo, Z.; Hertogen, J.; Liu, J.; Pasteels, P.; Boven, A.; Punzalan, L.; He, H.; Luo, X.; Zhang, W. Potassic Magmatism in Western Sichuan and Yunnan Provinces, SE Tibet, China: Petrological and Geochemical Constraints on Petrogenesis. *J. Petrol.* **2004**, *46*, 33–78. [CrossRef]
3. Prelević, D.; Foley, S.F.; Romer, R.L.; Cvetković, V.; Downes, H. Tertiary Ultrapotassic Volcanism in Serbia: Constraints on Petrogenesis and Mantle Source Characteristics. *J. Petrol.* **2005**, *46*, 1443–1487. [CrossRef]
4. Sokół, K.; Halama, R.; Meliksetian, K.; Savov, I.P.; Navasardyan, G.; Sudo, M. Alkaline magmas in zones of continental convergence: The Tezhsar volcano-intrusive ring complex, Armenia. *Lithos* **2018**, *320–321*, 172–191. [CrossRef]
5. Turner, S.; Arnaud, N.; Liu, J.; Rogers, N.; Hawkesworth, C.; Harris, N.; Kelley, S.; Van Calsteren, P.; Deng, W. Post-collision, Shoshonitic Volcanism on the Tibetan Plateau: Implications for Convective Thinning of the Lithosphere and the Source of Ocean Island Basalts. *J. Petrol.* **1996**, *37*, 45–71. [CrossRef]
6. Prelević, D.; Akal, C.; Foley, S.F.; Romer, R.L.; Stracke, A.; Van Den Bogaard, P. Ultrapotassic Mafic Rocks as Geochemical Proxies for Post-collisional Dynamics of Orogenic Lithospheric Mantle: The Case of Southwestern Anatolia, Turkey. *J. Petrol.* **2012**, *53*, 1019–1055. [CrossRef]
7. Conceição, R.V.; Green, D.H. Derivation of potassic (shoshonitic) magmas by decompression melting of phlogopite + pargasite lherzolite. *Lithos* **2004**, *72*, 209–229. [CrossRef]
8. Condamine, P.; Médard, E. Experimental melting of phlogopite-bearing mantle at 1 GPa: Implications for potassic magmatism. *Earth Planet. Sci. Lett.* **2014**, *397*, 80–92. [CrossRef]
9. Foley, S. Petrological characterization of the source components of potassic magmas: Geochemical and experimental constraints. *Lithos* **1992**, *28*, 187–204. [CrossRef]
10. Chen, J.; Henderson, C.M.B.; Foland, K.A. Open-System, Sub-Volcanic Magmatic Evolution: Constraints on the Petrogenesis of the Mount Brome Alkaline Complex, Canada. *J. Petrol.* **1994**, *35*, 1127–1153. [CrossRef]
11. Brown, P.E.; Becker, S.M. Fractionation, hybridisation and magma-mixing in the Kialineq centre East Greenland. *Contrib. Mineral. Petrol.* **1986**, *92*, 57–70. [CrossRef]
12. Litvinovsky, B.A.; Jahn, B.M.; Zanvilevich, A.N.; Saunders, A.; Poulain, S.; Kuzmin, D.V.; Reichow, M.K.; Titov, A.V. Petrogenesis of syenite–granite suites from the Bryansky Complex (Transbaikalia, Russia): Implications for the origin of A-type granitoid magmas. *Chem. Geol.* **2002**, *189*, 105–133. [CrossRef]
13. Jung, S.; Hoernes, S.; Hoffer, E. Petrogenesis of Cogenetic Nepheline and Quartz Syenites and Granites (Northern Damara Orogen, Namibia): Enriched Mantle versus Crustal Contamination. *J. Geol.* **2005**, *113*, 651–672. [CrossRef]
14. Jung, S.; Hoffer, E.; Hoernes, S. Neo-Proterozoic rift-related syenites (Northern Damara Belt, Namibia): Geochemical and Nd-Sr-Pb-O isotope constraints for mantle sources and petrogenesis. *Lithos* **2007**, *96*, 415–435. [CrossRef]
15. Riishuus, M.S.; Peate, D.W.; Tegner, C.; Wilson, J.R.; Brooks, C.K.; Waight, T.E. Petrogenesis of syenites at a rifted continental margin: Origin, contamination and interaction of alkaline mafic and felsic magmas in the Astrophyllite Bay Complex, East Greenland. *Contrib. Mineral. Petrol.* **2005**, *149*, 350–371. [CrossRef]
16. Yang, J.H.; Wu, F.Y.; Wilde, S.A.; Chen, F.; Liu, X.M.; Xie, L.W. Petrogenesis of an alkali syenite–granite–rhyolite suite in the Yanshan fold and thrust belt, Eastern North China Craton: Geochronological, geochemical and Nd–Sr–Hf isotopic evidence for lithospheric thinning. *J. Petrol.* **2008**, *49*, 315–351. [CrossRef]
17. Zhao, G.; Cawood, P.A. Precambrian geology of China. *Precambrian Res.* **2012**, *222–223*, 13–54. [CrossRef]
18. Kusky, T.M.; Polat, A.; Windley, B.F.; Burke, K.C.; Dewey, J.F.; Kidd, W.S.F.; Maruyama, S.; Wang, J.P.; Deng, H.; Wang, Z.S.; et al. Insights into the tectonic evolution of the North China Craton through comparative tectonic analysis: A record of outward growth of Precambrian continents. *Earth-Sci. Rev.* **2016**, *162*, 387–432. [CrossRef]
19. Gao, S.; Rudnick, R.L.; Carlson, R.W.; McDonough, W.F.; Liu, Y.S. Re-Os evidence for replacement of ancient mantle lithosphere beneath the North China craton. *Earth Planet. Sci. Lett.* **2002**, *198*, 307–322. [CrossRef]
20. Zheng, J.P.; Sun, M.; Zhou, M.-F.; Robinson, P. Trace elemental and PGE geochemical constraints of Mesozoic and Cenozoic peridotitic xenoliths on lithospheric evolution of the North China Craton. *Geochim. Cosmochim. Acta* **2005**, *69*, 3401–3418. [CrossRef]
21. Wu, F.-Y.; Walker, R.J.; Yang, Y.-H.; Yuan, H.-L.; Yang, J.-H. The chemical-temporal evolution of lithospheric mantle underlying the North China Craton. *Geochim. Cosmochim. Acta* **2006**, *70*, 5013–5034. [CrossRef]
22. Menzies, M.; Xu, Y.; Zhang, H.; Fan, W. Integration of geology, geophysics and geochemistry: A key to understanding the North China Craton. *Lithos* **2007**, *96*, 1–21. [CrossRef]
23. Chen, L.; Cheng, C.; Wei, Z. Seismic evidence for significant lateral variations in lithospheric thickness beneath the central and western North China Craton. *Earth Planet. Sci. Lett.* **2009**, *286*, 171–183. [CrossRef]
24. Wu, M.; Samson, I.M.; Qiu, K.; Zhang, D. Concentration mechanisms of Rare Earth Element-Nb-Zr-Be mineralization in the Baerzhe deposit, NE China: Insights from textural and chemical features of amphibole and rare-metal minerals. *Econ. Geol.* **2021**, *116*, 651–679. [CrossRef]

25. Chen, L. Concordant structural variations from the surface to the base of the upper mantle in the North China Craton and its tectonic implications. *Lithos* **2010**, *120*, 96–115. [CrossRef]
26. Huang, Y.-Q.; Wu, M.-Q.; Germain, B.; Yu, H.-C.; Qiao, B.-X.; Zhao, Z.-G.; Qiu, K.-F. Geodynamic setting and ore formation of the Younusisayi thorium deposit in the Altyn orogenic belt, NW China. *Ore Geol. Rev.* **2021**, *140*, 104552. [CrossRef]
27. Goldfarb, R.J.; Mao, J.-W.; Qiu, K.-F.; Goryachev, N. The great Yanshanian metallogenic event of eastern Asia: Consequences from one hundred million years of plate margin geodynamics. *Gondwana Res.* **2021**, *100*, 223–250. [CrossRef]
28. Chen, B.; Tian, W.; Zhai, M.G.; Arakawa, Y. Zircon U–Pb geochronology and geochemistry of the Mesozoic magmatism in the Taihang Mountains and other places of the North China Craton, with implications for petrogenesis and geodynamic setting. *Acta Petrol. Sin.* **2005**, *21*, 13–24.
29. Sun, W.; Ding, X.; Hu, Y.-H.; Li, X.-H. The golden transformation of the Cretaceous plate subduction in the west Pacific. *Earth Planet. Sci. Lett.* **2007**, *262*, 533–542. [CrossRef]
30. Zheng, J.P. Comparison of mantle-derived materials from different spatiotemporal settings: Implications for destructive and accretional processes of the North China Craton. *Chin. Sci. Bull.* **2009**, *54*, 3397–3416. [CrossRef]
31. Liang, Y.W.; Lai, Y.; Hu, H.; Zhang, F. Zircon U-Pb Ages and Geochemical Characteristics Study of Syenite from Weishan REE Deposit, Western Shandong. *Acta Sci. Nat. Univ. Pekin.* **2017**, *53*, 652–666. [CrossRef]
32. Liu, H.; Yu, L.; Chen, H.J.; Qiu, C.G.; Luo, H.D.; Yu, L.S.; Gao, Y.X. Zircon U-Pb Geochronology, Geochemistry and Geological Significance of Guandimiao Complex Intrusion in the East China Craton. *Miner. Depos.* **2022**, *in press*.
33. Lan, T.G.; Fan, H.-R.; Hu, F.-F.; Tomkins, A.G.; Yang, K.-F.; Liu, Y.S. Multiple crust-mantle interactions for the destruction of the North China Block: Geochemical and Sr-Nd-Pb-Hf isotopic evidence from the Longbaoshan alkaline complex. *Lithos* **2011**, *122*, 87–106. [CrossRef]
34. Wei, P.; Yu, X.; Li, D.; Liu, Q.; Yu, L.; Li, Z.; Geng, K.; Zhang, Y.; Sun, Y.; Chi, N. Geochemistry, Zircon U–Pb Geochronology, and Lu-Hf Isotopes of the Chishan Alkaline Complex, Western Shandong, China. *Minerals* **2019**, *9*, 293. [CrossRef]
35. Xia, Q.; Chen, Y. REE characteristics and ore source studies of Longbaoshan complex. *Geophys. Geochem. Explor.* **2002**, *26*, 110–117.
36. Xi, Z.-C.; Qiu, K.-F.; Zhi, C.-L.; Li, S.-S.; Shang, Z.; Huang, Y.-Q. Partial Melting of Lithospheric Mantle and Formation of the Early Cretaceous Alkaline Rocks in the Guandimiao REE Deposit, Luxi Terrane, Eastern China. *Minerals* **2022**, *12*, 670. [CrossRef]
37. Guo, F.; Fan, W.; Wang, Y.; Lin, G. Geochemistry of late Mesozoic mafic magmatism in west Shandong Province, eastern China: Characterizing the lost lithospheric mantle beneath the North China Block. *Geochem. J.* **2003**, *37*, 63–77. [CrossRef]
38. Hu, Q.-Y.; Li, L.; Tang, Z.-B.; Shi, X.-P. Characteristics and mechanism of Late Mesozoic extensional faults in West Shandong Uplift. *Geol. China* **2009**, *36*, 1233–1244. (In Chinese)
39. Song, M.C.; Yu, X.S.; Song, Y.X.; Xiao, B.J.; Zhou, D.S.; Gao, C.S.; Feng, A.P. Types, sources, and regional crust-mantle evolution background of diamonds in the western Shandong Province. *Acta Geol. Sin.* **2020**, *94*, 2606–2625.
40. Zhu, R.; Zhang, H.; Zhu, G.; Meng, Q.; Fan, H.; Yang, J.; Wu, F.; Zhang, Z.; Zheng, T. Craton destruction and related resources. *Int. J. Earth Sci.* **2017**, *106*, 2233–2257. [CrossRef]
41. Zeng, Q.; Wang, Y.; Yang, J.; Guo, Y.; Yu, B.; Zhou, L.; Qiu, H. Spatial–temporal distribution and tectonic setting of gold deposits in the Northern margin gold belt of the North China Craton. *Int. Geol. Rev.* **2020**, *63*, 941–972. [CrossRef]
42. Yang, J.-H.; Wu, F.-Y.; Wilde, S.A.; Belousova, E.; Griffin, W.L. Mesozoic decratonization of the North China block. *Geology* **2008**, *36*, 467–470. [CrossRef]
43. Zhu, G.; Jiang, D.; Zhang, B.; Chen, Y. Destruction of the eastern North China Craton in a backarc setting: Evidence from crustal deformation kinematics. *Gondwana Res.* **2012**, *22*, 86–103. [CrossRef]
44. Yu, X.; Fang, M.; Han, Z. Study on Ore-forming Series and Mineralization of the Guilaizhuang Gold Field in Western Shandong. *Acta Geol. Sin.* **2009**, *83*, 55–63.
45. Qiu, K.-F.; Yu, H.-C.; Deng, J.; Mclntire, D.; Gou, Z.-Y.; Geng, J.-Z.; Chang, Z.-S.; Zhu, R.; Li, K.-N.; Goldfarb, R. The giant Zaozigou Au-Sb deposit in West Qinling, China: Magmatic- or metamorphic-hydrothermal origin? *Miner. Depos.* **2020**, *18*, 345–362. [CrossRef]
46. Qiu, K.-F.; Goldfarb, R.J.; Deng, J.; Yu, H.-C.; Gou, Z.-Y.; Ding, Z.-J.; Wang, Z.-K.; Li, D.-P. Chapter 35: Gold Deposits of the Jiaodong Peninsula, Eastern China. In *Geology of the World's Major Gold Deposits and Provinces*; Society of Economic Geologists: Littleton, CO, USA, 2020; Volume 23, pp. 753–773. [CrossRef]
47. Yu, H.C.; Qiu, K.F.; Simon, A.; Wang, D.; Mathur, R.; Wan, R.Q.; Jiang, X.Y.; Deng, J. Telescoped boiling and cooling mechanisms triggered hydrothermal stibnite precipitation: Insights from the world's largest antimony deposit in Xikuangshan China. *Am. Mineral.* **2022**. [CrossRef]
48. Yu, H.-C.; Qiu, K.-F.; Deng, J.; Zhu, R.; Mathieu, L.; Sai, S.-X.; Sha, W.-J. Exhuming and Preserving Epizonal Orogenic Au-Sb Deposits in Rapidly Uplifting Orogenic Settings. *Tectonics* **2022**, *41*, e2021TC007165. [CrossRef]
49. Long, Z.-Y.; Qiu, K.-F.; Santosh, M.; Yu, H.-C.; Jiang, X.-Y.; Zou, L.-Q.; Tang, D.-W. Fingerprinting the metal source and cycling of the world's largest antimony deposit in Xikuangshan, China. *GSA Bull.* **2022**. [CrossRef]
50. Zhao, G.; Wilde, S.A.; Cawood, P.A.; Sun, M. Archean blocks and their boundaries in the North China Craton: Lithological, geochemical, structural and P–T path constraints and tectonic evolution. *Precambrian Res.* **2001**, *107*, 45–73. [CrossRef]

51. Zhang, H.-F.; Sun, M.; Zhou, X.-H.; Ying, J.-F. Geochemical constraints on the origin of Mesozoic alkaline intrusive complexes from the North China Craton and tectonic implications. *Lithos* **2005**, *81*, 297–317. [CrossRef]
52. Wang, J.F.; Xu, R.; An, M.G.; Xu, C.; Huang, K.P. Analysis on Metallogenic Geological Characteristics and Prospecting Prospects of Rare Earth Deposits in Longbaoshan Area in Shandong Province. *Shandong Land Resour.* **2020**, *36*, 1–12.
53. Yu, H.-C.; Qiu, K.-F.; Hetherington, C.J.; Chew, D.; Huang, Y.-Q.; He, D.-Y.; Geng, J.-Z.; Xian, H.-Y. Apatite as an alternative petrochronometer to trace the evolution of magmatic systems containing metamict zircon. *Contrib. Mineral. Petrol.* **2021**, *176*, 68. [CrossRef]
54. Geng, J.-Z.; Qiu, K.-F.; Gou, Z.-Y.; Yu, H.-C. Tectonic regime switchover of Triassic Western Qinling Orogen: Constraints from LA-ICP-MS zircon U–Pb geochronology and Lu–Hf isotope of Dangchuan intrusive complex in Gansu, China. *Geochemistry* **2017**, *77*, 637–651. [CrossRef]
55. Liu, Y.; Gao, S.; Hu, Z.; Gao, C.; Zong, K.; Wang, D. Continental and Oceanic Crust Recycling-induced Melt-Peridotite Interactions in the Trans-North China Orogen: U-Pb Dating, Hf Isotopes and Trace Elements in Zircons from Mantle Xenoliths. *J. Petrol.* **2009**, *51*, 537–571. [CrossRef]
56. Ludwig, K.R. *User's Manual for Isoplot v. 3.0: A Geochronological Toolkit for Microsoft Excel*; Berkeley Geochronology Center: Berkeley, CA, USA, 2003; Volume 4, p. 70.
57. Anderson, T. Correction of common lead in U-Pb analyses that do not report ^{204}Pb. *Chem. Geol.* **2002**, *192*, 59–79. [CrossRef]
58. Zhang, S.-H.; Zhao, Y.; Li, X.-H.; Ernst, R.E.; Yang, Z.-Y. The 1.33–1.30 Ga Yanliao large igneous provice in the North China Craton: Implications for reconstruction of the Nuna (Columbia) supercontinent, and specifically with the North Australian Craton. *Earth Planet. Sci. Lett.* **2017**, *465*, 112–125. [CrossRef]
59. Sun, S.S.; McDonough, W.F. Chemical and isotopic systematics of oceanic basalts: Implications for mantle composition and processes. In *Magmatism in the Ocean Basins*; Saunders, A.D., Norry, M.J., Eds.; Geological Society Publishing: London, UK, 1989; Volume 42, pp. 313–345.
60. Middlemost, E.A.K. Naming materials in the magma/igneous rock system. *Earth-Sci. Rev.* **1994**, *37*, 215–224. [CrossRef]
61. Maniar, P.D.; Piccoli, P.M. Tectonic discrimination of granitoids. *Geol. Soc. Am. Bull.* **1989**, *101*, 635–643. [CrossRef]
62. Peccerillo, A.; Taylor, S.R. Geochemistry of eocene calc-alkaline volcanic rocks from the Kastamonu area, Northern Turkey. *Contrib. Mineral. Petrol.* **1976**, *58*, 63–81. [CrossRef]
63. Yang, J.-H.; Xu, L.; Sun, J.-F.; Zeng, Q.; Zhao, Y.-N.; Wang, H.; Zhu, Y.-S. Geodynamics of decratonization and related magmatism and mineralization in the North China Craton. *Sci. China Earth Sci.* **2021**, *64*, 1409–1427. [CrossRef]
64. Zhou, W.W. Chronological, Petrological and Geochemical Characteristics of the Late Mesozoic Alkaline-Rich Intrusive Rocks along Tanlu Fault Zone. Master's Thesis, China University of Geosciences, Wuhan, China, 2014.
65. Pilet, S.; Baker, M.B.; Stolper, E.M. Metasomatized Lithosphere and the Origin of Alkaline Lavas. *Science* **2008**, *320*, 916–919. [CrossRef]
66. Zhu, Y.-X.; Wang, L.-X.; Xiong, Q.-H.; Ma, C.-Q.; Zhang, X.; Zhang, C.; Ahmed, H.A. Origin and evolution of ultrapotassic intermediate magma: The Songxian syenite massif, Central China. *Lithos* **2020**, *366–367*, 105554. [CrossRef]
67. Guillot, M.G.; Escayola, M.; Acevedo, R.; Pimentel, M.; Seraphim, G.; Proenza, J.; Schalamuk, I. The Plutón Diorítico Moat: Mildly alkaline monzonitic magmatism in the Fuegian Andes of Argentina. *J. South Am. Earth Sci.* **2009**, *28*, 345–359. [CrossRef]
68. Campbell, I.H.; Stepanov, A.S.; Liang, H.-Y.; Allen, C.M.; Norman, M.; Zhang, Y.-Q.; Xie, Y.-W. The origin of shoshonites: New insights from the Tertiary high-potassium intrusions of eastern Tibet. *Contrib. Mineral. Pet.* **2014**, *167*, 983. [CrossRef]
69. Li, S.-S.; Zeng, W.; Zhang, H.-F.; Wang, L.; Shivute, E.T.; Qiu, K.-F. Fractional Crystallization and Partial Melting of the Paleoproterozoic Gneisses and Pegmatite in the Giant Husab Uranium Deposit, Namibia. *Minerals* **2022**, *12*, 379. [CrossRef]
70. Jiang, Y.-H.; Liu, Z.; Jia, R.-Y.; Liao, S.-Y.; Zhou, Q.; Zhao, P. Miocene potassic granite–syenite association in western Tibetan Plateau: Implications for shoshonitic and high Ba–Sr granite genesis. *Lithos* **2012**, *134–135*, 146–162. [CrossRef]
71. Fan, W.-M.; Guo, F.; Wang, Y.-J.; Lin, G.; Zhang, M. Post-orogenic bimodal volcanism along the Sulu orogenic belt in Eastern China. *Phys. Chem. Earth Part A Solid Earth Geodesy* **2001**, *26*, 733–746. [CrossRef]
72. Wang, S.J.; Wan, Y.S.; Zhang, C.J.; Yang, E.X.; Song, Z.Y.; Wang, L.F.; Wang, J.G. Forming ages of early Precambrian metamorphic strata in Shandong Province—Proofs of zircon SHRIMP U–Pb dating. *Shandong Land Resour.* **2009**, *25*, 18–24.
73. Jahn, B.-M.; Wu, F.Y.; Lo, C.-H.; Tsai, C.-H. Crust–mantle interaction induced by deep subduction of the continental crust: Geochemical and Sr–Nd isotopic evidence from post-collisional mafic–ultramafic intrusions of the northern Dabie complex, central China. *Chem. Geol.* **1999**, *157*, 119–146. [CrossRef]
74. La Flèche, M.; Camiré, G.; Jenner, G.A. Geochemistry of post-Acadian, Carboniferous continental intraplate basalts from the Maritimes Basin, Magdalen Islands, Québec, Canada. *Chem. Geol.* **1998**, *148*, 115–136. [CrossRef]
75. Zheng, Y.; Xu, Z.; Zhao, Z.; Dai, L. Mesozoic mafic magmatism in North China: Implications for thinning and destruction of cratonic lithosphere. *Sci. China Earth Sci.* **2018**, *61*, 353–385. [CrossRef]
76. Furukawa, Y.; Tatsumi, Y. Melting of a subducting slab and production of high-mg andesite magmas: Unusual magmatism in SW Japan at 13∼15 Ma. *Geophys. Res. Lett.* **1999**, *26*, 2271–2274. [CrossRef]
77. Kamei, A.; Owada, M.; Nagao, T.; Shiraki, K. High-Mg diorites derived from sanukitic HMA magmas, Kyushu Island, southwest Japan arc: Evidence from clinopyroxene and whole rock compositions. *Lithos* **2004**, *75*, 359–371. [CrossRef]

78. Barth, M.G.; McDonough, W.F.; Rudnick, R.L. Tracking the budget of Nb and Ta in the continental crust. *Chem. Geol.* **2000**, *165*, 197–213. [CrossRef]
79. Gao, S.; Luo, T.-C.; Zhang, B.-R.; Zhang, H.-F.; Han, Y.-W.; Zhao, Z.-D.; Hu, Y.-K. Chemical composition of the continental crust as revealed by studies in East China. *Geochim. Cosmochim. Acta* **1998**, *62*, 1959–1975. [CrossRef]
80. Turner, S.; Caulfield, J.; Turner, M.; Van Keken, P.; Maury, R.; Sandiford, M.; Prouteau, G. Recent contribution of sediments and fluids to the mantle's volatile budget. *Nat. Geosci.* **2011**, *5*, 50–54. [CrossRef]
81. De Souza, Z.S.; Martin, H.; Peucat, J.-J.; de Sá, E.F.J.; de Freitas Macedo, M.H. Calc-Alkaline Magmatism at the Archean Proterozoic Transition: The Caicoó Complex Basement (NE Brazil). *J. Petrol.* **2007**, *48*, 2149–2185. [CrossRef]
82. Gorman, P.J.; Kerrick, D.M.; Connolly, J.A.D. Modeling open system metamorphic decarbonation of subducting slabs. *Geochem. Geophys. Geosyst.* **2006**, *7*, Q04007. [CrossRef]
83. Labanieh, S.; Chauvel, C.; Germa, A.; Quidelleur, X. Martinique: A Clear Case for Sediment Melting and Slab Dehydration as a Function of Distance to the Trench. *J. Petrol.* **2012**, *53*, 2441–2464. [CrossRef]
84. Yang, W.-B.; Niu, H.-C.; Shan, Q.; Chen, H.Y.; Hollings, P.; Li, N.-B.; Yan, S.; Zartman, R.E. Geochemistry of primary-carbonate bearing K-rich igneous rocks in the Awulale Mountains, western Tianshan: Implications for carbon-recycling in subduction zone. *Geochim. Cosmochim. Acta* **2014**, *143*, 143–164. [CrossRef]
85. Foley, S.F.; Wheller, G.E. Parallels in the origin of the geochemical signatures of island arc volcanics and continental potassic igneous rocks: The role of residual titanates. *Chem. Geol.* **1990**, *85*, 1–18. [CrossRef]
86. Foley, S.; Peccerillo, A. Potassic and ultrapotassic magmas and their origin. *Lithos* **1992**, *28*, 181–185. [CrossRef]
87. Zhang, L.-C.; Zhou, X.-H.; Ying, J.-F.; Wang, F.; Guo, F.; Wan, B.; Chen, Z.-G. Geochemistry and Sr-Nd-Pb-Hf isotopes of Early Cretaceous basalts from the Great Xinggan Range, NE China: Implications for their origin and mantle source characteristics. *Chem. Geol.* **2008**, *256*, 12–23. [CrossRef]
88. Li, X.-H. Cretaceous magmatism and lithospheric extension in Southeast China. *J. Asian Earth Sci.* **2000**, *18*, 293–305. [CrossRef]
89. Xu, W.-L.; Pei, F.-P.; Wang, F.; Meng, E.; Ji, W.-Q.; Yang, D.-B.; Wang, W. Spatial–temporal relationships of Mesozoic volcanic rocks in NE China: Constraints on tectonic overprinting and transformations between multiple tectonic regimes. *J. Asian Earth Sci.* **2013**, *74*, 167–193. [CrossRef]
90. Li, J.; Zhang, Y.; Dong, S.; Johnston, S.T. Cretaceous tectonic evolution of South China: A preliminary synthesis. *Earth-Sci. Rev.* **2014**, *134*, 98–136. [CrossRef]
91. Liu, C.; Zhu, G.; Zhang, S.; Gu, C.; Li, Y.; Su, N.; Xiao, S. Mesozoic strike-slip movement of the Dunhua–Mishan Fault Zone in NE China: A response to oceanic plate subduction. *Tectonophysics* **2018**, *723*, 201–222. [CrossRef]
92. Guo, L.; Wang, T.; Zhang, J.; Liu, J.; Qi, G.; Li, J. Evolution and time of formation of the Hohhot metamorphic core complex, North China: New structural and geochronologic evidence. *Int. Geol. Rev.* **2012**, *54*, 1309–1331. [CrossRef]
93. Li, Y.; Zhu, G.; Su, N.; Xiao, S.; Zhang, S.; Liu, C.; Xie, C.; Yin, H.; Wu, X. The Xiaoqinling metamorphic core complex: A record of Early Cretaceous backarc extension along the southern part of the North China Craton. *GSA Bull.* **2019**, *132*, 617–637. [CrossRef]
94. Zhu, R.X.; Xu, Y.G.; Zhu, G.; Zhang, H.F.; Xia, Q.K.; Zheng, T.Y. Destruction of the North China Craton. *Sci. China Earth Sci.* **2012**, *55*, 1565–1587. [CrossRef]
95. Wang, Y.; Zhou, L.; Liu, S.; Li, J.; Yang, T. Post-cratonization deformation processes and tectonic evolution of the North China Craton. *Earth-Sci. Rev.* **2018**, *177*, 320–365. [CrossRef]
96. Zhang, S.-H.; Zhao, Y.; Davis, G.A.; Ye, H.; Wu, F. Temporal and spatial variations of Mesozoic magmatism and deformation in the North China Craton: Implications for lithospheric thinning and decratonization. *Earth-Sci. Rev.* **2013**, *131*, 49–87. [CrossRef]
97. Zhu, G.; Liu, C.; Gu, C.; Zhang, S.; Li, Y.; Su, N.; Xiao, S. Oceanic plate subduction history in the western Pacific Ocean: Constraint from late Mesozoic evolution of the Tan-Lu Fault Zone. *Sci. China Earth Sci.* **2018**, *61*, 386–405. [CrossRef]
98. Zhu, R.; Fan, H.; Li, J.; Meng, Q.; Li, S.; Zeng, Q. Decratonic gold deposits. *Sci. China Earth Sci.* **2015**, *58*, 1523–1537. [CrossRef]
99. Pearce, J.A.; Harris, N.B.W.; Tindle, A.G. Trace Element Discrimination Diagrams for the Tectonic Interpretation of Granitic Rocks. *J. Petrol.* **1984**, *25*, 956–983. [CrossRef]
100. Li, S.-R.; Santosh, M. Metallogeny and craton destruction: Records from the North China Craton. *Ore Geol. Rev.* **2013**, *56*, 376–414. [CrossRef]
101. Whalen, J.B.; Currie, K.L.; Chappell, B.W. A-type granites: Geochemical characteristics, discrimination and petrogenesis. *Contrib. Mineral. Petrol.* **1987**, *95*, 407–419. [CrossRef]
102. Müller, D.; Rock, N.M.S.; Groves, D.I. Geochemical discrimination between shoshonitic and potassic volcanic rocks in different tectonic settings: A pilot study. *Mineral. Petrol.* **1992**, *46*, 259–289. [CrossRef]
103. Li, Y.; Xu, W.-L.; Wang, F.; Pei, F.-P.; Tang, J.; Zhao, S. Triassic volcanism along the eastern margin of the Xing'an Massif, NE China: Constraints on the spatial–temporal extent of the Mongol–Okhotsk tectonic regime. *Gondwana Res.* **2017**, *48*, 205–223. [CrossRef]
104. Pearce, J.A.; Norry, M.J. Petrogenetic implications of Ti, Zr, Y, and Nb variations in volcanic rocks. *Contrib. Mineral. Petrol.* **1979**, *69*, 33–47. [CrossRef]
105. Yang, D.-B.; Xu, W.-L.; Zhao, G.-C.; Huo, T.-F.; Shi, J.-P.; Yang, H.-T. Tectonic implications of Early Cretaceous low-Mg adakitic rocks generated by partial melting of thickened lower continental crust at the southern margin of the central North China Craton. *Gondwana Res.* **2016**, *38*, 220–237. [CrossRef]

106. Ma, L.; Jiang, S.-Y.; Hou, M.-L.; Dai, B.-Z.; Jiang, Y.-H.; Yang, T.; Zhao, K.-D.; Pu, W.; Zhu, Z.-Y.; Xu, B. Geochemistry of Early Cretaceous calc-alkaline lamprophyres in the Jiaodong Peninsula: Implication for lithospheric evolution of the eastern North China Craton. *Gondwana Res.* **2014**, *25*, 859–872. [CrossRef]
107. Jiang, Y.-H.; Jiang, S.-Y.; Ling, H.-F.; Ni, P. Petrogenesis and tectonic implications of Late Jurassic shoshonitic lamprophyre dikes from the Liaodong Peninsula, NE China. *Mineral. Petrol.* **2010**, *100*, 127–151. [CrossRef]